



HAL
open science

A unified single-field Volume-of-Fluid-based formulation for multi-component interfacial transfer with local volume changes

Julien Maes, Cyprien Soulaine

► To cite this version:

Julien Maes, Cyprien Soulaine. A unified single-field Volume-of-Fluid-based formulation for multi-component interfacial transfer with local volume changes. *Journal of Computational Physics*, 2020, 402, pp.109024. 10.1016/j.jcp.2019.109024 . insu-02426952

HAL Id: insu-02426952

<https://insu.hal.science/insu-02426952v1>

Submitted on 24 Nov 2020

HAL is a multi-disciplinary open access archive for the deposit and dissemination of scientific research documents, whether they are published or not. The documents may come from teaching and research institutions in France or abroad, or from public or private research centers.

L'archive ouverte pluridisciplinaire **HAL**, est destinée au dépôt et à la diffusion de documents scientifiques de niveau recherche, publiés ou non, émanant des établissements d'enseignement et de recherche français ou étrangers, des laboratoires publics ou privés.

A unified single-field Volume-of-Fluid-based formulation for multi-component interfacial transfer with local volume changes

Julien Maes^a, Cyprien Soulaine^b

^a*Institute of GeoEnergy Engineering, Heriot-Watt University, Edinburgh, U.K.*

^b*French Geological Survey, BRGM, Orléans, France*

Abstract

This paper presents a novel unified single-field formulation for Volume-Of-Fluid simulation of interfacial mass transfer with local volume changes. By comparison with the previous models referred as Continuous Species Transfer in the literature, our improved model uses a single-field formulation of the local mass transfer across the interface, enabling us to take into account local volume changes induced by non-dilute species transfer. The numerical model, implemented in our in-house OpenFOAM-based simulator, is validated by comparison with analytical solutions in 1D and 2D, and a semi-analytical solution in 3D. The implemented approach is first applied to investigate competing mass transfer in an infinite cylinder. We then simulate the shrinking of a single-component rising bubble at low Schmidt number. The numerical model is shown to be well adapted to investigate local Sherwood numbers and existing correlation for mass transfer at fluid interfaces.

Keywords: Interface, Mass transfer, Multicomponent fluid, Local volume change, Volume-Of-Fluid, OpenFOAM

1. Introduction

Interface species transfers are present in a wide range of applications such as acid gas treatment, bubble column reactors and geological storage of CO₂ in aquifers. These processes include viscous and capillary effects, chemical reactions and the coupling between mass transfer and fluid dynamics. For such complex systems, analytical solution are only restricted to very simple geometries and flow conditions (Danckwerts, 1970; Hadamard, 1911; Coutelieris et al., 2006). In addition, experimental studies are often time-consuming, hard to control, and quantities of interest may be difficult to measure during the course of the experiment. Numerical simulation is therefore a powerful tool to investigate these processes and achieve optimal design and process control.

Numerical simulation of interfacial mass transfer can be done using Direct Numerical Simulation (DNS) of the Navier-Stokes Equation (NSE), for which mass and momentum conservation are directly solved without model simplification. DNS of two-phase flow can be performed using the Volume-Of-Fluid (VOF) method, for which the interface between the two fluids is captured using an indicator function, which is a phase volume fraction (Hirt and Nichols, 1981). Although other methods such as level-set (Sussman et al., 1994; Chai et al., 2017; Gibou et al., 2018; Luo et al., 2019) can provide a more accurate description of the sharp interface, the VOF method is attractive due to its flexibility, robustness in terms of mass conservation, and adaptability to more complex physic.

VOF methods can be geometric or algebraic, depending on how the computation of the interface curvature and the advection of the indicator function are performed. Geometric methods explicitly reconstruct the interface, and the advection of the indicator function is performed based on a geometric representation of the faces flux (Gerlach et al., 2006; Weymouth and Yue, 2010; Owkes and Desjardins, 2014). Geometric methods do not create numerical diffusion and can achieve better precision with accurate interface reconstruction (Popinet, 2009), but their application to unstructured mesh is highly demanding and scarcely used (Maric et al., 2013). Alternatively, algebraic methods perform the advection of the indicator function by numerically solving a transport equation

40 (Hirt and Nichols, 1981). Algebraic methods can be easily applied to unstructured grids as no explicit interface
41 reconstruction is needed. The main challenge is to preserve a sharp interface while maintaining the boundedness
42 of the phase volume fraction. High resolution differencing schemes and models with compression of the interface
43 are generally introduced to reduce this problem (Zalesak, 1979; Ubbink and Issa, 1999).

44 To simulate species transfer in two-phase systems within the VOF method, two conceptually different ap-
45 proaches have been developed, namely the two-field and single-field approaches. The main criterion to decide
46 which approach to use is to ensure consistency of the advection operator for phase fraction and species con-
47 centration, otherwise artificial mass transfer arises (Deising et al., 2016). In the two-field approach, the species
48 concentration in each phase is solved separately, using two concentration fields - one per phase - which are set to
49 zero when continued in the other phase (Bothe and Fleckenstein, 2013). Consistent advection of phase fraction
50 and species concentration can only be achieved if the interface is geometrically advected. Therefore, the two-field
51 approach is consistent in principles with any geometric VOF method. In the single-field approach, a mixture quan-
52 tity, obtain by volume averaging of species concentration, is transported by solving an algebraic equation (Haroun
53 et al., 2010; Deising et al., 2016). Therefore, the single-field approach is consistent in principles with interface
54 advection for any algebraic VOF method, and has been applied with high resolution differencing schemes (Haroun
55 et al., 2010; Deising et al., 2016, 2018) and models with compression of the interface (Yang et al., 2017; Graveleau
56 et al., 2017; Maes and Soullaine, 2018). Hence, if a geometric VOF method is employed, the two-field approach
57 should be used. On the other side, if an algebraic VOF method is employed, then the single-field approach should
58 be used.

59 Both two-field and single-field approaches exhibit method-specific advantages and disadvantages. Within the
60 two-field approach, a sub-grid model based on the reconstructed interface can be used to reduce the resolution
61 required around the interface (Bothe and Fleckenstein, 2013). Within the single-field approach, the inclusion
62 of sub-grid scale models is complex and requires further research. Another benefit of the two-field approach is
63 that the concentration gradients are readily available, which allows for calculating local mass transfer across the
64 interface in a straightforward manner, and enabled Fleckenstein and Bothe (2015) to extend the model to include
65 local volume changes for non-dilute mass transfer. However, since the two-field approach is only consistent with
66 geometric VOF method, applying the method to complex unstructured grids is challenging. On the other side,
67 applying the single-field approach on unstructured grids is straightforward, since it is consistent in principles with
68 any algebraic VOF method (Marschall et al., 2012; Deising et al., 2016). This is essential for some application
69 such as pore-scale simulation of CO₂ storage in the subsurface (Graveleau et al., 2017) or pore-scale simulation of
70 enhanced oil recovery (Maes and Geiger, 2018). Another advantage of the single-field approach is that it is fully
71 consistent with the micro-continuum formulation for modelling multiscale transport in porous media (Soullaine
72 et al., 2018, 2019)

73 However, no model exists to include local volume changes for non-dilute mass transfer within the single-field
74 approach. Contrary to the two-field approach, the information about the one-sided interface concentrations and
75 one-sided concentration gradients is inherently lost and need to be recovered with numerical modelling. Soh et al.
76 (2017a,b) applied the two-field approach to an algebraic VOF model by reconstructing the phase concentration
77 gradient at the interface. Although this formulation ensures continuity of the chemical potential, it does not ensure
78 continuity of the species mass flux (convective and diffusive) across the interface, and artificial mass transfer
79 arises. Up to now, there is no consistent model to compute the local mass transfer. The objective of the present
80 work is to correct this problem in order to simulate interface transfer during two-phase flow with local volume
81 changes using the single-field formulation. The main contribution is the derivation of a single-field numerical
82 model of the interface transfer and local Sherwood number (Section 2.4) and its application to gas dissolution in
83 liquid solvent, something that could only be done with the two-field approach before.

84 The paper is organised as follows. The governing equations and numerical models including the computation
85 of the local mass transfer are presented in Section 2. In Section 3, the model is validated by comparison with

analytical solutions in 1D and 2D and a semi-analytical solution in 3D. Finally, the model is applied to simulate competing mass transfer in an infinite cylinder and mass transfer during rising of a single-component gas bubble at low Schmidt number.

2. Mathematical model

In this section, we introduce the model used to simulate two-phase flow with local volume change. First, we present the governing equations in the physical continuous domain. Then, we derive the grid-based VOF equations used to simulate the movement of a fluid/fluid interface along with multicomponent mass transfer on a discrete Eulerian mesh. Finally, we discuss the numerical implementation and the post-processing procedure.

2.1. Governing equations in the continuous physical space

This section presents the basic continuum hydrodynamic laws that govern multiphase flow with interface transfer. The domain is decomposed into two disjoint subsets, namely the disperse (gas) phase Ω_d and the continuous (liquid) phase Ω_c , separated by the interface Σ (see Figure 1a). Each phase is assumed to be Newtonian and in-

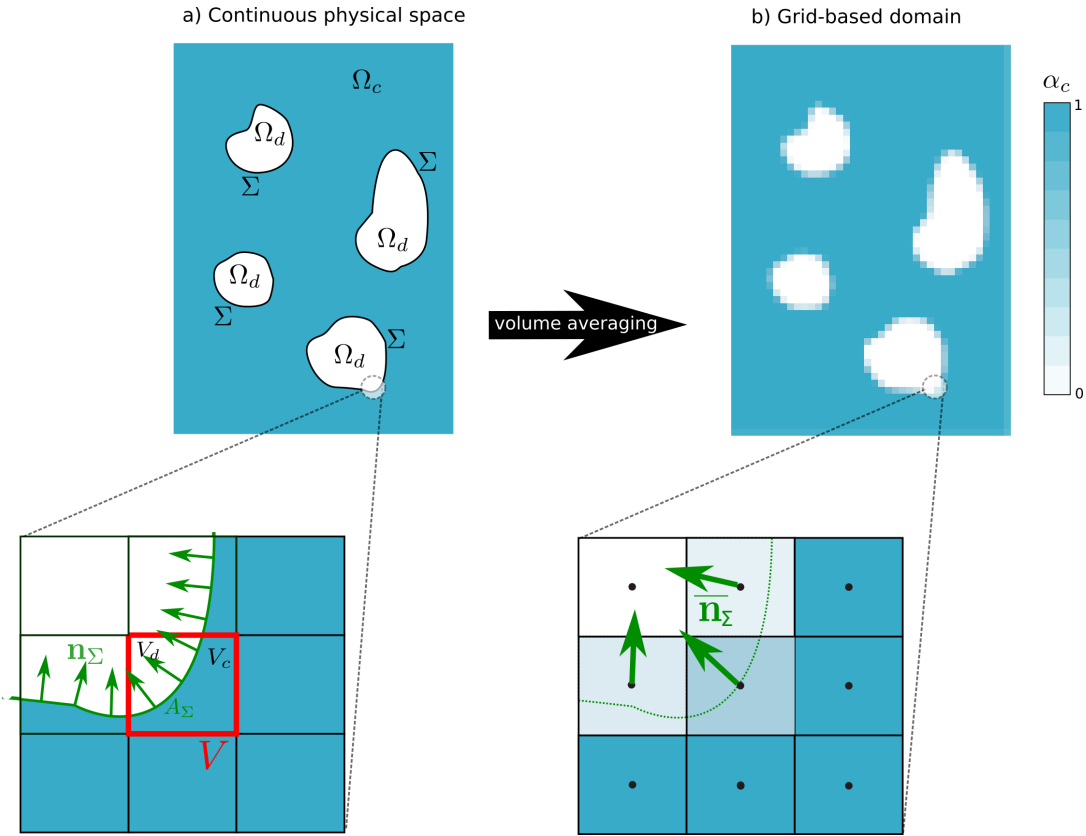


Figure 1: Distribution of the fluid phases in (a) the continuous physical domain, (b) the discrete Eulerian grid.

compressible, and fluid properties are assumed to be constant in each phase (in particular independent of the phase composition). Therefore, mass conservation in each phase writes

$$\nabla \cdot \mathbf{u}_i = 0 \quad \text{in } \Omega_i, i = d, c, \quad (1)$$

where \mathbf{u}_i is the velocity of phase i . Mass conservation at the fluid/fluid interface writes

$$[[\rho_i (\mathbf{u}_i - \mathbf{w}) \cdot \mathbf{n}_\Sigma]] = 0 \quad \text{at } \Sigma, \quad (2)$$

101 where ρ_i is the density of phase i , \mathbf{w} is the velocity of the interface, \mathbf{n}_Σ is the normal vector to the fluid/fluid
 102 interface from the continuous to the disperse phase, and the double brackets describe a jump at the interface. In
 103 addition, the momentum conservation under the classical NSE formulation writes

$$\rho_i \left(\frac{\partial \mathbf{u}_i}{\partial t} + \mathbf{u}_i \cdot \nabla \mathbf{u}_i \right) = -\nabla p_i + \nabla \cdot \mathbf{S}_i + \rho_i \mathbf{g} \quad \text{in } \Omega_i, i = d, c, \quad (3)$$

104 where \mathbf{g} is the gravity vector, $\mathbf{S}_i = \mu_i (\nabla \mathbf{u}_i + \nabla \mathbf{u}_i^T)$ is the viscous stress tensor, and p_i and μ_i are the pressure and
 105 viscosity of phase i , respectively. Momentum conservation at the fluid/fluid interface writes

$$\llbracket p_i \mathbf{l} - \mathbf{S}_i \rrbracket \cdot \mathbf{n}_\Sigma = \sigma \kappa \mathbf{n}_\Sigma \quad \text{at } \Sigma, \quad (4)$$

106 where \mathbf{l} is the unity tensor, σ is the interfacial tension and $\kappa = -\nabla \cdot \mathbf{n}_\Sigma$ is the interface curvature.

107 Both phases are assumed to be composed of a mixture of n components. We assume that component n is the
 108 solvent of the continuous phase, and that all other species present in the continuous phase are dilute. Furthermore,
 109 we assume that component n is not soluble in the disperse phase. Therefore, the concentration c_{ji} of species j in
 110 phase i satisfies

$$\sum_{1 \leq j < n} c_{j,d} = \rho_d, \quad \sum_{1 \leq j \leq n} c_{j,c} = \rho_c. \quad (5)$$

111 In the absence of homogeneous chemical reactions, conservation of mass of species j in phase i is described by
 112 the standard advection-diffusion equation

$$\frac{\partial c_{ji}}{\partial t} + \nabla \cdot (c_{ji} \mathbf{u}_i + \mathbf{J}_{ji}) = 0 \quad \text{in } \Omega_i, \quad (6)$$

113 where \mathbf{J}_{ji} is the mass flux of component j in phase i by diffusion. For all dilute components in the system, the
 114 diffusive mass flux can be modelled using Fick's law (Taylor and Krishna, 1993). This applies to every component
 115 in the continuous phase but component n . The diffusive flux of n in phase c can be obtained using

$$\mathbf{J}_{n,c} = - \sum_{1 \leq j < n} \mathbf{J}_{j,c}. \quad (7)$$

116 However, we do not need to solve the mass conservation of component n since closure is obtained using the mass
 117 conservation of each phase (Eq. 1). Finally, we assume that the diffusive flux of species in the disperse phase can
 118 also be modelled using Fick's law. This is true for the two cases simulated here, namely a single-component and
 119 a binary disperse mixture. Therefore, for all components simulated in the system, the mass flux by diffusion can
 120 be modelled using

$$\mathbf{J}_{ji} = -D_{ji} \nabla c_{ji}, \quad (8)$$

121 where D_{ji} is the molecular diffusion coefficient of component j in phase i . At the interface, mass conservation
 122 imposes continuity of mass fluxes on each side

$$\llbracket (c_{ji} (\mathbf{u}_i - \mathbf{w}) + \mathbf{J}_{ji}) \cdot \mathbf{n}_\Sigma \rrbracket = 0 \quad \text{at } \Sigma. \quad (9)$$

123 Finally, thermodynamics equilibrium imposes equality of chemical potential at the interface. This is model here
 124 using Henry's law

$$c_{j,c} = H_j c_{j,d} \quad \text{on } \Sigma, \quad (10)$$

125 where H_j is the Henry's coefficient for component j , assumed constant here for simplicity.

126 *2.2. Algebraic VOF Method: from continuous to discrete domain*

127 The mathematical model introduced in the former section is defined on a continuous physical domain. The
 128 computational procedure to solve this system of equations, however, relies on the Finite Volume Method (FVM)
 129 (Patankar, 1980), i.e. a discretization of the domain into an ensemble of subset volumes. In FVM, the partial
 130 differential equations representing conservation laws (Eqs. (1), (3) and (6)) are transformed into discrete algebraic
 131 equations by integrating them over each discrete volume, V . This operation is carried out using the averaging
 132 operator,

$$\overline{\beta}_i = \frac{1}{V} \int_{V_i} \beta_i dV, \quad (11)$$

133 where β_i is a function defined in Ω_i ($i = c, d$) and $V_i = V \cap \Omega_i$. The application of the volume average operator to
 134 the indicator function $\mathbb{1}_i$ (which is equal to 1 in Ω_i and 0 elsewhere) defines the volume fraction, α_i , of phase i in
 135 the finite volume V ,

$$\alpha_i = \frac{1}{V} \int_{V_i} \mathbb{1}_i dV. \quad (12)$$

136 α_i is used as the phase indicator function in the FVM grid. In cells that contain the disperse phase only, $\alpha_d = 1$. In
 137 cells that contain the continuous phase only, $\alpha_d = 0$. In cells crossed by the fluid-fluid interface Σ , $0 < \alpha_d < 1$ (see
 138 Figure 1b). Tracking the evolution of α_i is the cornerstone of the Volume-of-Fluid technique used in this paper. In
 139 VOF, this is achieved by solving conservation laws for the single-field (global variable) quantity, β , defined as

$$\beta = \alpha_d \widetilde{\beta}_d + \alpha_c \widetilde{\beta}_c. \quad (13)$$

140 where the phase average over phase i is defined as

$$\widetilde{\beta}_i = \frac{1}{V_i} \int_{V_i} \beta_i dV. \quad (14)$$

141 The single-field β is defined all over the computational grid regardless the nature of the phase that occupies the
 142 cells (disperse, continuous or mixture). The VOF methods solve partial differential equations that govern the
 143 single-field velocity \mathbf{u} , the single-field pressure p and the single-field concentration c_j for species j . Likewise, the
 144 viscosity μ and density ρ are defined as single-field variables.

145 The governing equations on the FVM grid are obtained by applying the volume averaging operator, Eq. (11),
 146 to the continuity equations, Eq. (1), to the momentum equations, Eq. (3), and to the species conservation laws,
 147 Eq. (6), for the continuous and the disperse phases, and then by adding the two phase-averaged equations to form
 148 the governing equation for the single-field variable. In the averaging process, the volume averaging operator
 149 is applied to the spatial differential operators (gradient and divergence). This operation is not straightforward
 150 because integrals and derivatives can not be interchanged in volumes that contain the fluid-fluid interface Σ . This
 151 is achieved using the spatial volume averaging theorems (Whitaker, 1999),

$$\begin{aligned} \overline{\nabla \beta}_i &= \nabla \overline{\beta}_i + \frac{1}{V} \int_{A_\Sigma} \beta_i \mathbf{n}_\Sigma dA, \\ \overline{\nabla \cdot \beta}_i &= \nabla \cdot \overline{\beta}_i + \frac{1}{V} \int_{A_\Sigma} \beta_i \cdot \mathbf{n}_\Sigma dA, \end{aligned} \quad (15)$$

152 where $A_\Sigma = V \cap \Sigma$ is the surface area of the interface within the control volume V . The surface integral term in
 153 these equations transforms the boundary conditions at the discontinuity Σ between the two fluids phases into a
 154 body force. For example, the integration of the continuity equations gives rise to the volume source term,

$$\dot{m} = \frac{1}{V} \int_{A_\Sigma} \rho_i (\mathbf{u}_i - \mathbf{w}) \cdot \mathbf{n}_\Sigma dA, \quad (16)$$

155 that describes the rate of phase change within a control volume V , i.e. the amount of mass that is transferred from
 156 the continuous phase to the disperse phase (and reverse) across the fluid-fluid interface.

157 In the VOF method, the normal vector \mathbf{n}_Σ defined on every points of the discontinuity Σ is transformed into a
 158 mean normal surface that is computed using the gradient of the phase indicator function (Quintard and Whitaker,
 159 1994),

$$\nabla\alpha_d = \frac{1}{V} \int_{A_\Sigma} \mathbf{n}_\Sigma dA. \quad (17)$$

160 Therefore, the average of the normal vector \mathbf{n}_Σ is understood as

$$\bar{\mathbf{n}}_\Sigma = \frac{\nabla\alpha_d}{\|\nabla\alpha_d\|}. \quad (18)$$

161 $\bar{\mathbf{n}}_\Sigma$ is a unit vector defined at the cell centres that describes the mean normal to the fluid-fluid interface in a control
 162 volume. In particular, it is used to compute the mean interface curvature.

163 The single-field equations are obtained following the averaging procedure described above. Here, we present
 164 only the final conservation laws. A detailed derivation can be found in Fleckenstein and Bothe (2015). The
 165 continuity equation reads

$$\nabla \cdot \mathbf{u} = \dot{m} \left(\frac{1}{\rho_d} - \frac{1}{\rho_c} \right). \quad (19)$$

166 Further, the single-field momentum equation can be written as

$$\frac{\partial \rho \mathbf{u}}{\partial t} + \nabla \cdot (\rho \mathbf{u} \mathbf{u}) = -\nabla p + \nabla \cdot (\mu (\nabla \mathbf{u} + \nabla \mathbf{u}^T)) + \rho \mathbf{g} + \mathbf{f}_\Sigma, \quad (20)$$

167 where

$$\mathbf{f}_\Sigma = \frac{1}{V} \int_{A_\Sigma} \sigma \kappa \mathbf{n}_\Sigma dA \quad (21)$$

168 is the mean surface tension force described as a body force. To compute \mathbf{f}_Σ , the curvature within the control volume
 169 is approximated by a mean curvature estimated from the normal vector, $\kappa = -\nabla \cdot \bar{\mathbf{n}}_\Sigma$ (Brackbill et al., 1992). The
 170 surface tension σ and the mean curvature are then constant within a control volume, and can be removed from the
 171 integral. Therefore, using Eq. (17), \mathbf{f}_Σ becomes

$$\mathbf{f}_\Sigma = \sigma \kappa \nabla \alpha_d. \quad (22)$$

172 This surface tension force model is known as Continuous Surface Force (CSF) (Brackbill et al., 1992). Since in
 173 the VOF method, the fluid interface is represented by an indicator function which changes over a thin region, the
 174 estimation of the curvature using the CSF method is inaccurate and can generate non-physical parasitic velocities
 175 (Scardovelli and Zaleski, 1999; Popinet, 2018). These spurious currents might be reduced by computing the
 176 curvature from a smoothed indicator function $\widehat{\alpha}_d$, i.e.

$$\begin{aligned} \kappa &= \nabla \cdot \left(\frac{\nabla \widehat{\alpha}_d}{\|\nabla \widehat{\alpha}_d\|} \right), \\ \widehat{\alpha}_d &= \frac{\sum_f \alpha_{d_f} A_f}{\sum_f A_f}, \end{aligned} \quad (23)$$

177 where α_{d_f} is the value of α_d on the face f of the control volume, obtained by linear interpolation, and A_f is the
 178 face surface area.

179 Finally, the volumetric phase equation is

$$\frac{\partial \alpha_d}{\partial t} + \nabla \cdot (\alpha_d \mathbf{u}) + \nabla \cdot (\alpha_d \alpha_c \mathbf{u}_r) = \frac{\dot{m}}{\rho_d}, \quad (24)$$

180 where $\mathbf{u}_r = \widetilde{\mathbf{u}}_d - \widetilde{\mathbf{u}}_c$ is the relative velocity. This advection equation is exact because its derivation does not
 181 imply any assumption (Fleckenstein and Bothe, 2015). Note that the last term on the left-hand side has non-
 182 zero value only in the cells containing the fluid/fluid interface. The relative velocity \mathbf{u}_r is a consequence of mass
 183 and momentum transfer between the phases. However, Fleckenstein and Bothe (2015) showed that \mathbf{u}_r may be
 184 neglected even in the case of very good solubility (e.g. CO₂ in water) in order to simplify Eq. (24).

185 High resolution differencing schemes such as Flux Corrected Transport (FCT) (Zalesak, 1979) or Normalised
 186 Variable Formulation (NVF) (Leonard, 1988) can be used to reduce the smearing of the interface. These methods
 187 combined a bounded but diffusive low-order scheme with an unbounded but more accurate higher order scheme.
 188 In order to maintain a sharp interface, the amount of downwinding should be maximised, leading to so-called in-
 189 terface capturing schemes such as the Compressive Interface Capturing Scheme for Arbitrary Meshes (CICSAM)
 190 (Ubbink and Issa, 1999) and the High Resolution Interface Capturing (HRIC) scheme (Muzaferija et al., 1999).
 191 However, the present work is based on the *interFoam* solver (OpenCFD, 2016), which algebraic advection im-
 192 plementation utilises a FCT method called Multidimensional Universal Limiter with Explicit Solution (MULES)
 193 (Weller, 2006). In addition, compression of the interface is performed but, rather than using an interface capturing
 194 scheme, an artificial compression term is introduced by replacing \mathbf{u}_r in Eq. (24) by a compressive velocity \mathbf{u}_{comp} ,
 195 normal to the interface and with an amplitude based on the maximum of the single-field velocity (Rusche, 2002)

$$\mathbf{u}_r \equiv \mathbf{u}_{comp} = \bar{\mathbf{n}}_\Sigma \left[\min \left(c_\alpha \frac{|\phi_f|}{A_f}, \max_f \left(\frac{|\phi_f|}{A_f} \right) \right) \right], \quad (25)$$

196 where c_α is the compression constant (generally between 0 and 4) and ϕ_f is the volumetric flux across f . In all
 197 our simulations, we choose $c_\alpha = 1.0$.

198 2.3. Single-field concentration equation

199 Similarly, applying volume-averaging to the mass conservation equation of each component in each phase,
 200 and then adding them up, yields to the single-field concentration equation. Deising et al. (2016) proposed a formal
 201 derivation of the model, leading to the so-called Continuous Species Transfer (CST) formulation

$$\frac{\partial c_j}{\partial t} + \nabla \cdot \mathbf{F}_j + \nabla \cdot \mathbf{J}_j = 0, \quad (26)$$

202 where the advective flux is

$$\mathbf{F}_j = \alpha_d \widetilde{c}_{j,d} \widetilde{\mathbf{u}}_d + \alpha_c \widetilde{c}_{j,c} \widetilde{\mathbf{u}}_c, \quad (27)$$

203 and the diffusive flux is

$$\mathbf{J}_j = -\alpha_d D_{j,d} \nabla \widetilde{c}_{j,d} - \alpha_c D_{j,c} \nabla \widetilde{c}_{j,c}. \quad (28)$$

204 In the single-field approach, the fluxes \mathbf{F}_j and \mathbf{J}_j have to be described in term of single-field variables. Haroun
 205 et al. (2010) proposed the following formulation for the diffusion flux

$$\mathbf{J}_j = -D_j^{SF} \nabla c_j + \Phi_j, \quad (29)$$

206 where D_j^{SF} is the single-field diffusion coefficient and Φ_j is the CST flux, defined as

$$\Phi_j = (1 - H_j) D_j^{SF} \frac{c_j}{\alpha_d + H_j \alpha_c} \nabla \alpha_d. \quad (30)$$

207 The debate regarding the best formulation for the single-field diffusion coefficient was initiated in the original
 208 work of Haroun et al. (2010) and pursued in Marschall et al. (2012) and Deising et al. (2016). Indeed, Haroun

209 et al. (2010) first proposed an arithmetic mean for the diffusion coefficient

$$D_j^{SF} \equiv D_j^a = \alpha_d D_{j,d} + \alpha_c D_{j,c}. \quad (31)$$

210 However, they showed in their own test cases that a harmonic mean was more accurate. Further, Deising et al.
211 (2016) derived the following formulation for the diffusive flux

$$\mathbf{J}_j = -D_j^a \nabla c_j - \alpha_d \alpha_c \frac{(D_{j,d} - D_{j,c})(1 - H_j)}{\alpha_d + H_j \alpha_c} \nabla c_j + \Phi_j, \quad (32)$$

212 with

$$\Phi_j = \frac{c_j}{\alpha_d + H_j \alpha_c} \left((D_{j,d} - H_j D_{j,c}) - \frac{H_j (D_{j,d} - D_{j,c})}{\alpha_d + H_j \alpha_c} \right) \nabla \alpha_d. \quad (33)$$

213 They compared this formulation to the harmonic formulation on several test cases and obtained almost identical
214 results. However, Eqs. (32)-(33) can be drastically simplified by putting everything over the common denominator
215 $\alpha_d + H_j \alpha_c$. Doing so, we can show that this formulation is equivalent to Haroun et al. (2010) formulation (Eqs.
216 (29)-(30)) if the arithmetic mean diffusion is replaced by the equilibrium-based mean diffusion

$$D_j^{SF} \equiv D_j^m = \frac{\alpha_d D_{j,d} + H_j \alpha_c D_{j,c}}{\alpha_d + H_j \alpha_c}, \quad (34)$$

217 which states that the diffusion of component j in the interface region is equal to the weighted mean of the phase
218 diffusion coefficients $D_{j,d}$ and $D_{j,c}$ weighted by α_d and $H_j \alpha_c$. This formulation has many advantages over the
219 arithmetic and harmonic formulations proposed by Haroun et al. (2010); Marschall et al. (2012); Deising et al.
220 (2016). It is an equivalent simplified formulation of Eqs. (26)-(33) that ensures continuity of the diffusive flux
221 of dilute species at the interface and that, contrary to the harmonic formulation, can be applied to the case when
222 $D_{j,i} \rightarrow 0$ (for example when the disperse phase is pure).

223 Finally, the advective flux can be written as (Maes and Soulaire, 2018)

$$\mathbf{F}_j = c_j \mathbf{u} + \alpha_d \alpha_c (\tilde{c}_{j,d} - \tilde{c}_{j,c}) \mathbf{u}_r. \quad (35)$$

224 Since the CST model (Eqs.(26)-(35)) has been derived by volume averaging, it is in principles consistent with
225 the phase advection equation (Eq.1), regardless of the discretization scheme employed. However, Deising et al.
226 (2016) noted that to obtain a fully consistent advection scheme and avoid artificial mass transfer at the interface,
227 it is essential to apply the same discretization scheme to all advected quantities. Following this principle, the CST
228 method has been applied successfully with algebraic VOF methods with FCT (Haroun et al., 2010) or CICSAM
229 (Deising et al., 2018) discretization schemes.

230 When using high resolution discretization schemes, the relative velocity \mathbf{u}_r may be neglected, so the advective
231 flux in the CST model becomes $\mathbf{F}_j = c_j \mathbf{u}$. However, additional care must be taken when using the CST model
232 with an artificial compressive velocity. Yang et al. (2017) neglected the relative velocity in the species transport
233 equation, and they observed that, when convection dominates diffusion locally near the interface, this formulation
234 generates a large numerical error. They show that in order to capture the discontinuity at the interface accurately,
235 the mesh should be designed so that the diffusion dominates the advection locally. This is described by the local
236 Péclet number $Pe_{local} = \frac{U \delta_x}{D}$, and they recommend to use $Pe_{local} < 0.5$. However, this restriction cannot be applied
237 for the case when $D_{j,i} \rightarrow 0$ (for example when the disperse phase is pure). Maes and Soulaire (2018) shows that
238 the numerical error is in fact due to inconsistency in the phase and component advection schemes arising from the
239 compression term. It is therefore essential to use the so called Compressive CST (C-CST) (Maes and Soulaire,

240 2018) formulation, where the advective flux includes a compressive term

$$\mathbf{F}_j = c_j \mathbf{u} + \alpha_d \alpha_c (\widetilde{c}_{j,d} - \widetilde{c}_{j,c}) \mathbf{u}_{comp}. \quad (36)$$

241 The phase concentration $\widetilde{c}_{j,d}$ and $\widetilde{c}_{j,c}$ are unknown and need to be expressed as a function of α_d and c_j . In the
 242 original C-CST model (Maes and Soulaïne, 2018), the phase concentration are assumed to be at equilibrium in the
 243 grid blocks that contain the interface, and $\widetilde{c}_{j,d} = \frac{c_j}{\alpha_d + H_j \alpha_c}$ and $\widetilde{c}_{j,c} = \frac{H_j c_j}{\alpha_d + H_j \alpha_c}$. The phase concentration difference
 244 was,

$$(\widetilde{c}_{j,d} - \widetilde{c}_{j,c}) = \frac{(1 - H_j) c_j}{\alpha_d + H_j \alpha_c}. \quad (37)$$

245 In the present paper, we propose a different model based on the computation of the gradient of concentration at
 246 the interface. Using the definition of the single-field concentration, we have,

$$\begin{aligned} \nabla c_j \cdot \nabla \alpha_d &= \nabla (\alpha_d \widetilde{c}_{j,d} + \alpha_c \widetilde{c}_{j,c}) \cdot \nabla \alpha_d, \\ &= [\alpha_d \nabla \widetilde{c}_{j,d} + \alpha_c \nabla \widetilde{c}_{j,c} + (\widetilde{c}_{j,d} - \widetilde{c}_{j,c}) \nabla \alpha_d] \cdot \nabla \alpha_d, \\ &= \alpha_d \nabla \widetilde{c}_{j,d} \cdot \nabla \alpha_d + \alpha_c \nabla \widetilde{c}_{j,c} \cdot \nabla \alpha_d + (\widetilde{c}_{j,d} - \widetilde{c}_{j,c}) \|\nabla \alpha_d\|^2. \end{aligned} \quad (38)$$

247 Although the gradient of the phase concentration across the interface is zero only when the phases are at chemical
 248 equilibrium in the cell, the compression may assume that they are in order to avoid additional mass transfer across
 249 the interface. Therefore, we assume $\nabla \widetilde{c}_{j,d} \cdot \nabla \alpha_d = \nabla \widetilde{c}_{j,c} \cdot \nabla \alpha_d = 0$. and the phase concentration difference can be
 250 written as

$$(\widetilde{c}_{j,d} - \widetilde{c}_{j,c}) = \frac{\nabla c_j \cdot \nabla \alpha_d}{\|\nabla \alpha_d\|^2}. \quad (39)$$

251 In the rest of the paper, this model is referred to as the normal C-CST model while the model using Eq. (37) is
 252 referred to as the original C-CST. The two C-CST models are compared for a 1D test case with infinite Péclet
 253 number in section 3. In particular, we observe that the local mass transfer between the phase generated by the
 254 compression is zero for the normal C-CST model but not for the original C-CST model. This is an essential
 255 property for computing interface mass transfer and local volume change.

256 2.4. Interface mass transfer

257 The VOF approach with local volume change requires the computation of the rate of mass transfer, \dot{m} , at the
 258 gas/liquid interface. Indeed, \dot{m} appears both in the continuity equation, Eq. (19), and in the phase conservation
 259 law, Eq. (24). By definition, the rate of mass transfer, responsible for the local phase volume change, results from
 260 the sum of the rate of transfer, \dot{m}_j , of all the species that cross the interface, i.e. all the species except for the one
 261 labelled n that remains always in the continuous phase. Hence, the rate of mass transfer writes

$$\dot{m} = \sum_{1 \leq j < n} \dot{m}_j, \quad (40)$$

262 where the rate of species transfer is defined in each control volume V that contains part of the interface Σ by
 263 integrating the flux condition Eq. (9) over the surface of the interface. We have,

$$\dot{m}_j = \dot{m}_{j,i} = \frac{1}{V} \int_{A_\Sigma} (c_{j,i} (\mathbf{u}_i - \mathbf{w}) - D_{j,i} \nabla c_{j,i}) \cdot \mathbf{n}_\Sigma dA. \quad (41)$$

264 This integral involves variables defined in the continuous physical space and needs to be formulated in terms of
 265 grid-based variables to be used in the VOF method. In a control volume, the concentration at the interface is
 266 assumed to verify $c_{j,i_\Sigma} \approx \widetilde{c}_{j,i}$ and $\nabla c_{j,i_\Sigma} \approx \nabla \widetilde{c}_{j,i}$ (Soulaïne et al., 2011). Because, $\widetilde{c}_{j,i}$ is a volume averaged quantity

267 over the control volume V , it has a constant value all along A_Σ and can be pull out the surface integral. Finally,
 268 using Eq. (16) and Eq. (17), we obtain

$$\begin{aligned}
 \dot{m}_{j,i} &= \frac{1}{V} \int_{A_\Sigma} (\widetilde{c}_{j,i} (\mathbf{u}_i - \mathbf{w}) - D_{j,i} \nabla \widetilde{c}_{j,i}) \cdot \mathbf{n}_\Sigma dA, \\
 &= \widetilde{c}_{j,i} \frac{1}{V} \int_{A_\Sigma} (\mathbf{u}_i - \mathbf{w}) \cdot \mathbf{n}_\Sigma dA - D_{j,i} \nabla \widetilde{c}_{j,i} \cdot \frac{1}{V} \int_{A_\Sigma} \mathbf{n}_\Sigma dA, \\
 &= \frac{\widetilde{c}_{j,i}}{\rho_i} \frac{1}{V} \int_{A_\Sigma} \rho_i (\mathbf{u}_i - \mathbf{w}) \cdot \mathbf{n}_\Sigma dA - D_{j,i} \nabla \widetilde{c}_{j,i} \cdot \frac{1}{V} \int_{A_\Sigma} \mathbf{n}_\Sigma dA, \\
 &= \frac{\widetilde{c}_{j,i}}{\rho_i} \dot{m} - D_{j,i} \nabla \widetilde{c}_{j,i} \cdot \nabla \alpha_d.
 \end{aligned} \tag{42}$$

269 Eq. (42) cannot be used in its present form since it depends on $\widetilde{c}_{j,i}$ that is not computed in the VOF method. It is
 270 recast into a form that depends only on the single-field variables using the sum of the species transfer rate on each
 271 side of the interface weighted by a fluid volume fraction. We have,

$$\begin{aligned}
 \dot{m}_j &= \alpha_d \dot{m}_{j,d} + \alpha_c \dot{m}_{j,c}, \\
 &= \alpha_d \left(\frac{\widetilde{c}_{j,d}}{\rho_d} \dot{m} - D_{j,d} \nabla \widetilde{c}_{j,d} \cdot \nabla \alpha_d \right) + \alpha_c \left(\frac{\widetilde{c}_{j,c}}{\rho_c} \dot{m} - D_{j,c} \nabla \widetilde{c}_{j,c} \cdot \nabla \alpha_d \right), \\
 &= \left(\alpha_d \frac{\widetilde{c}_{j,d}}{\rho_d} + \alpha_c \frac{\widetilde{c}_{j,c}}{\rho_c} \right) \dot{m} - \left(\alpha_d D_{j,d} \nabla \widetilde{c}_{j,d} + \alpha_c D_{j,c} \nabla \widetilde{c}_{j,c} \right) \cdot \nabla \alpha_d, \\
 &= X_j \dot{m} + \mathbf{J}_j \cdot \nabla \alpha_d,
 \end{aligned} \tag{43}$$

272 where $X_j = \left(\alpha_d \frac{\widetilde{c}_{j,d}}{\rho_d} + \alpha_c \frac{\widetilde{c}_{j,c}}{\rho_c} \right)$, and where the diffusion flux was simplified using Eqs. (28) and (29). Using Eq. (40)
 273 along with Eq. (43) we obtain

$$\dot{m} = \sum_{1 \leq j < n} X_j \dot{m} + \sum_{1 \leq j < n} \mathbf{J}_j \cdot \nabla \alpha_d. \tag{44}$$

274 To close the system, the sum $\sum_{1 \leq j < n} X_j$ is calculated using Eq. (5) along with the assumption that all the $1 \leq j < n$
 275 components are diluted in c so that $\rho_c \approx \widetilde{c}_{n,c}$. The sum of X_j writes,

$$\sum_{1 \leq j < n} X_j = \alpha_d + \alpha_c \left(1 - \frac{\widetilde{c}_{n,c}}{\rho_c} \right) \approx \alpha_d, \tag{45}$$

276 Therefore, using Eq. (29), the total mass transfer in a control volume that includes interfacial area is calculated as

$$\dot{m} = - \frac{\sum_{1 \leq j < n} (D_j^m \nabla c_j - \Phi_j)}{1 - \alpha_d} \cdot \nabla \alpha_d \tag{46}$$

277 This closes Eq. (24) and the entire system.

278 2.5. Numerical implementation

279 The numerical method has been implemented in our OpenFOAM[®]-based reactive transport solver (OpenCFD,
 280 2016). The standard VOF solver of OpenFOAM[®], so-called *interFoam* has been extended for this purpose into
 281 another solver called *interTransferFoam*. The full solution procedure is presented in Fig. 2. *interFoam* solves
 282 the system formed by Eq. (19), (24) and (20) on a collocated Eulerian grid. A pressure equation is obtained
 283 by combining the continuity (Eq. (19)) and momentum (Eq. (20)) equations. The system is then solved with a
 284 predictor-corrector strategy based on the Pressure Implicit Splitting Operator (PISO) algorithm (Issa et al., 1985).
 285 Three iterations of the PISO loop are used to stabilise the system. An explicit formulation is used to treat the
 286 coupling between the phase distribution equation (Eq. (24)) and the pressure equation. This imposes a limit on the

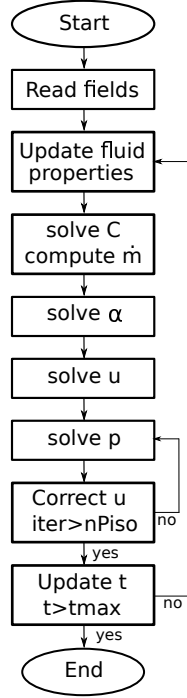


Figure 2: Full solution procedure for *interTransferFoam*.

time-step size by introducing a capillary wave time scale described by the Brackbill conditions (Brackbill et al., 1992).

In *interTransferFoam*, the concentration equation (Eq. (26)) is solved sequentially before the phase conservation. The interfacial mass transfer (Eq. (46)) is then computed and re-injected in the continuity (Eq. (19)) and phase equations (Eq. (24)). The space discretization of the convection terms is performed using the second-order *vanLeer* scheme (van Leer, 1974). For the compression terms, the interpolation of $\alpha_d \alpha_c$ is performed using the *interfaceCompression* scheme (OpenCFD, 2016). The diffusion term $\nabla \cdot (D_j^m \nabla c_j)$ is discretized using the Gauss linear limited corrected scheme, which is second order and conservative. The discretization of the CST flux is performed using the Gauss linear scheme.

For the computation of the mass transfer \dot{m} , we define

$$\Phi_D = \frac{\sum_{1 \leq j < n} D_j^m \nabla c_j - \Phi_j}{1 - \alpha_d} \quad (47)$$

and then we use $\Phi_D \cdot \nabla \alpha_d = \nabla \cdot (\Phi_D \alpha_d) - \alpha_d \nabla \cdot \Phi_D$. The discretization of $\Phi_D \alpha_d$ is performed using upwinding in the direction of $\nabla \alpha_d$ in order to prevent negative α_d . This is only first-order accurate (see Section 3), but all second-order discretization schemes available in OpenFOAM® have shown strong instabilities.

2.6. Dimensionless analysis and large-scale post-processing

In this section, we describe the dimensionless numbers used to analyse the simulation results in terms of bulk-averaged properties.

For two-phase flow, the relative importance of inertia and viscous forces is quantified using the Reynolds number Re , while the importance of gravity and surface tension force is characterised using the Eötvös Eo and Morton Mo numbers,

$$Re = \frac{\rho_c UL}{\mu_c}, \quad Eo = \frac{\Delta \rho g L^2}{\sigma}, \quad Mo = \frac{g \mu_c^4 \Delta \rho}{\rho_c^2 \sigma^3}, \quad (48)$$

306 where U and L are reference velocity and length, respectively.

307 Similarly, the relative importance of viscous and molecular diffusivity is quantified using the Schmidt number
308 Sc , while the Péclet number $Pe = Sc \times Re$ is equal to the ratio of advective to diffusive transport

$$Sc = \frac{\mu_c}{\rho_c D_{j,c}}, \quad Pe = \frac{UL}{D_{j,c}}. \quad (49)$$

309 A common engineering approach for the modelling of species transfer across interfaces is to introduce a
310 species transfer coefficient k_j

$$\int_{\Omega} \dot{m}_j dV = k_j A_{\Sigma} (H_j c_{j,d,\infty} - c_{j,c,\infty}), \quad (50)$$

311 where $c_{j,i,\infty}$ is the bulk average concentration of j in phase i . This leads to the definition of the Sherwood number
312 Sh , which quantifies the ratio of interface mass transfer rate to the molecular diffusion rate

$$Sh = \frac{k_j L}{D_{j,c}}. \quad (51)$$

313 Establishing accurate Sherwood correlation as a function of the other dimensionless groups (Reynolds, Schmidt,
314 Péclet) is one of the most investigated engineering question in bubble column reactors (Oellrich et al., 1973; Clift
315 et al., 1978; Takemura and Yabe, 1998).

316 3. Verification

317 3.1. Two-phase transport in a 1D tube at infinite Péclet number

318 The objective of this test case is to observe and quantify the artificial mass transfer that arises at the interface
319 when compression is not applied consistently for the phase volume fraction and species concentration. For this,
320 four numerical implementations are compared in OpenFOAM[®] (OpenCFD, 2016). First, no interface compression
321 is used. The advection is performed using the FCT method implemented in MULES (Weller, 2006), but the
322 compression is cancelled by setting $c_{\alpha} = 0$. The species concentration equation is modelled using the standard
323 CST method. This implementation is labelled VOF-FCT0-S-CST. Secondly, we used compression of the interface
324 for the phase fraction ($c_{\alpha} = 1$), but not for the species concentration. This implementation is labelled VOF-FCT1-
325 S-CST. Thirdly, we use compression of the interface for the phase fraction and for the species concentration, using
326 the original C-CST method (Eqs. (36) and (37)). This implementation is labelled VOF-FCT1-OC-CST. Finally,
327 we use compression of the interface for the phase fraction and for the species concentration, using the normal
328 C-CST method (Eqs. (36) and (39)). This implementation is labelled VOF-FCT1-NC-CST.

329 To compare the four implementations in terms of artificial mass transfer, we consider a 1D tube of length
330 $200 \mu\text{m}$. The tube is initially filled with the disperse phase ($\alpha_d = 1$) from $x=0$ to $40 \mu\text{m}$ and the continuous phase
331 ($\alpha_d = 0$) from $x=40$ to $200 \mu\text{m}$. The concentration of a species A is set to 1 kg/m^3 in the disperse phase and
332 0 in the continuous phase. The Henry coefficient H_A is assumed to be equal to 0.5 , so that the system is not at
333 equilibrium. The velocity is constant $U=0.05 \text{ m/s}$ in the domain. In addition, we assume that $D_{A,d} = D_{A,c} = 0$
334 (infinite Pe). Therefore, there is no transfer between the phase and the analytical solution for both phase fraction
335 and species concentration is a sharp front moving at speed U .

336 The simulation are performed on a regular grid with resolution $\Delta x = 1 \mu\text{m}$ and with a constant time-step
337 $\Delta t = 10^{-7} \text{ s}$. Fig. 3 shows the phase fraction and concentration profiles at different time for the four different
338 implementations and Fig. 4 shows the evolution of the fraction of component A in the continuous phase. For
339 the case with no compression (VOF-FCT0-S-CST), the interface is slightly smeared and spans over seven cells
340 (Fig. 3a). However, no artificial mass transfer is observed (Fig. 4). The advection operators for phase fraction
341 and species concentration are fully consistent. For the case where compression is applied to the phase fraction but

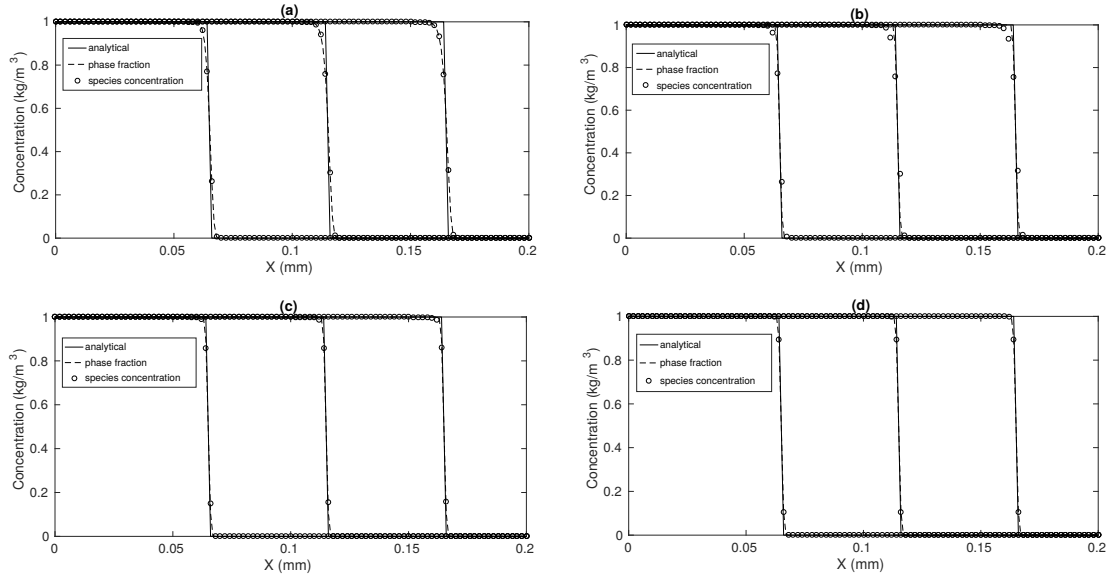


Figure 3: Concentration profile during two-phase transport in a 1D tube at different time obtained using (a) VOF-FCT0-S-CST, (b) VOF-FCT1-S-CST, (c) VOF-FCT1-OC-CST and (d) VOF-FCT1-NC-CST.

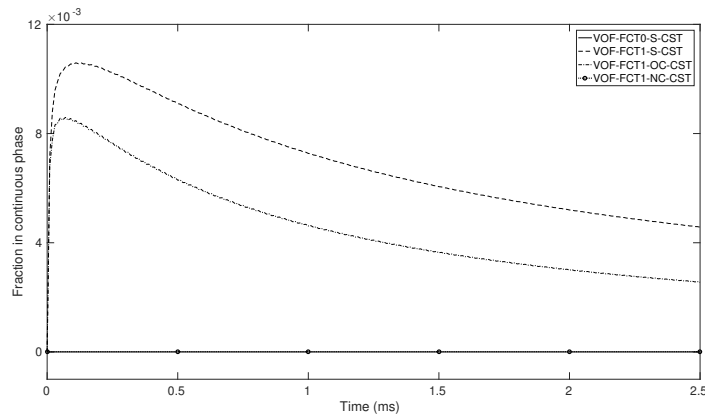


Figure 4: Evolution of the average concentration of component A in the continuous phase during two-phase transport in a 1D tube using the four different implementation of the VOF-CST methods. When compression is applied to the interface, the standard CST and the original C-CST model generate an erroneous transfer between the phases, while for the normal C-CST model, the concentration of A in the continuous phase remains zero.

342 not to the species concentration (VOF-FCT1-S-CST), the interface is sharper, spanning over three cells, but the
 343 species concentration is diffuse (Fig. 3b). The fraction of A in the continuous phase does not remain equal to zero,
 344 but reaches a maximum value of 0.01 at $t=0.15$ ms. The erroneous mass transfer between the phases is maximum
 345 at $t=0$, with value equal to $0.012 \text{ kg/m}^2/\text{s}$. This error corresponds to a diffusion coefficient of $1.2 \times 10^{-6} \text{ m}^2/\text{s}$.
 346 The advection operators for phase fraction and species concentration are not consistent. Next, when the original
 347 C-CST method is applied to the species concentration (VOF-FCT1-OC-CST), the species concentration is slightly
 348 less diffuse, but the problem is not fully corrected (Fig. 3c). Again, the fraction of A in the continuous phase
 349 does not remain equal to zero, but reaches a maximum value of 8×10^{-3} at $t=0.1$ ms. The erroneous mass transfer
 350 between the phases is also maximum at $t=0$, with the same value of $0.012 \text{ kg/m}^2/\text{s}$. In the original C-CST model,
 351 the phase concentration at the interface are obtained by assuming local equilibrium between the phases. However,
 352 when the phase concentrations deviate strongly from equilibrium, artificial mass transfer between the phases

353 arises. The original C-CST method is only consistent with artificial compression when phase concentrations at the
 354 interface are at equilibrium. In the present case, equilibrium is never reached since Pe is infinite. Finally, when
 355 the normal C-CST method is applied (VOF-FCT1-NC-CST), both phase fraction and species concentration are
 356 sharp, spanning over three cells (Fig. 3d), and no artificial mass transfer is observed. This is because the normal
 357 C-CST model is built so that no interface transfer is generated by the compression (Eq. (38)). This is an essential
 358 result when computing the interface mass transfer and the local volume change. The advection operators for phase
 359 fraction and species concentration are fully consistent. In the rest of the paper, we will use compression of the
 360 interface with the normal C-CST method.

361 3.2. Dissolution of a single-component gas phase into an immiscible liquid solvent in a semi-infinite tube

362 The objective of this test case is to validate the computation of the interface mass transfer and the local volume
 363 change by comparison with a system where an analytical solution exists. For this, we consider the case where the
 364 disperse phase is a single-component gas with $\rho_d = 1 \text{ kg/m}^3$ and the continuous phase is a binary liquid mixture
 365 with $\rho_c = 1000 \text{ kg/m}^3$. The species A of the disperse phase is a dilute component in phase c , with $H_A = 0.5$ and
 366 $D_{A,c} = 10^{-6} \text{ m}^2/\text{s}$. The second species is a solvent that is not soluble in d . The domain is a 1D semi-infinite tube
 367 (Fig. 5). The gas/liquid interface is initially positioned at a distance $l_0 = 0.5 \text{ mm}$ from the left boundary. Initially,
 the concentration of dilute species in the liquid is equal to zero.

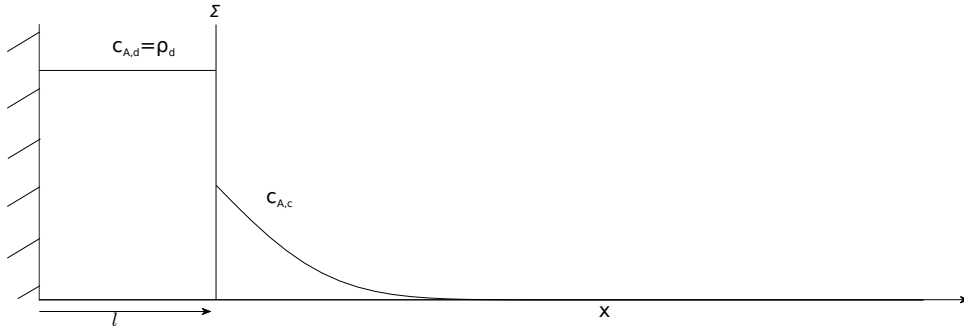


Figure 5: Set-up for dissolution of a single-component gas phase into an immiscible liquid solvent in a semi-infinite tube

368 Due to incompressibility, the velocity in each phase is constant, and equal to zero in the gas phase. Mass
 369 conservation at the interface (Eq. (2)) gives
 370

$$u_c = \frac{\rho_c - \rho_d}{\rho_c} w \quad \text{at } x = l. \quad (52)$$

371 Therefore, the mass conservation of the dilute component in c writes

$$\begin{aligned} \frac{\partial c_{A,c}}{\partial t} + \frac{\rho_c - \rho_d}{\rho_c} w \frac{\partial c_{A,c}}{\partial x} &= D_{A,c} \frac{\partial^2 c_{A,c}}{\partial x^2} & \text{for } x > l, \\ c_{A,c}(x, 0) &= 0 & \text{for } x > l, \\ c_{A,c}(l, t) &= H_A \rho_d & \text{for } t > 0, \\ \frac{dl}{dt} = w &= \frac{D_{A,c}}{\rho_d} \frac{\partial c_{A,c}}{\partial x} \Big|_{x=l} & \text{for } t > 0 \end{aligned} \quad (53)$$

372 Assuming that $\rho_d \ll \rho_c$, an analytical solution for Eq. (53) writes

$$c_{A,c}(x, t) = H_A \rho_d \left(1 - \operatorname{erf} \left(\frac{x-l}{2\sqrt{D_{A,c}t}} \right) \right) \quad \text{for } x > l, \quad (54)$$

$$l(t) = l_0 - 2H_A \rho_d \sqrt{\frac{D_{A,c}t}{\pi}}.$$

373 The simulations were performed on a domain of length 10 mm, to mimic a semi-infinite tube. In order to
374 investigate convergence, we define the dimensionless grid size

$$\Delta x^* = \frac{\Delta x}{l_0}, \quad (55)$$

375 and the error for concentration and interface position

$$\operatorname{Err}(c(\Delta x^*)) = \max_t \left(\sqrt{\int \left(\frac{c(\Delta x^*, t) - c(\Delta x^* \rightarrow 0, t)}{\rho_d} \right)^2 dt} \right), \quad (56)$$

$$\operatorname{Err}(l(\Delta x^*)) = \max_t \left(\frac{|l(\Delta x^*, t) - l(\Delta x^* \rightarrow 0, t)|}{l_0} \right).$$

376 Fig. 6 shows the evolution of the convergence errors with grid resolution. All simulations are performed with a
time-step of $0.2 \mu\text{s}$, for which they have all converged in time. We observe that both measures show first-order

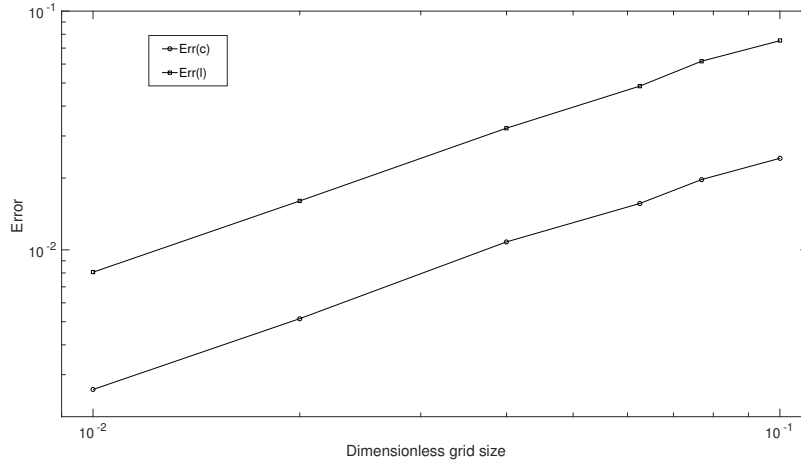


Figure 6: Evolution of convergence of concentration and interface position during dissolution of a single-component gas phase into an immiscible liquid solvent in a semi-infinite tube. Both measures show first-order convergence.

377
378 convergence. Although the CST model itself is second-order accurate, the discretization of the phase transfer
379 flux (Eq. 46) is performed using upwinding to avoid negative volume fraction. We have tested the second-order
380 accurate schemes included in OpenFOAM but they all show strong instabilities.

381 Fig. 7 show a comparison of analytical and numerical simulations for grid resolution $\Delta x^* = 0.01$. We observe
382 a very good agreement between the simulation and the exact solution. Both convergence errors (Eq. (56)) are
383 smaller than 0.01.

384 3.3. Growth of binary gas in infinite cylinder

385 The objective of this test case is to validate the computation of the local volume change when two species are
386 present in the gas phase. For this, we consider an infinite cylinder of radius $R = 1$ mm. The initial radius of the

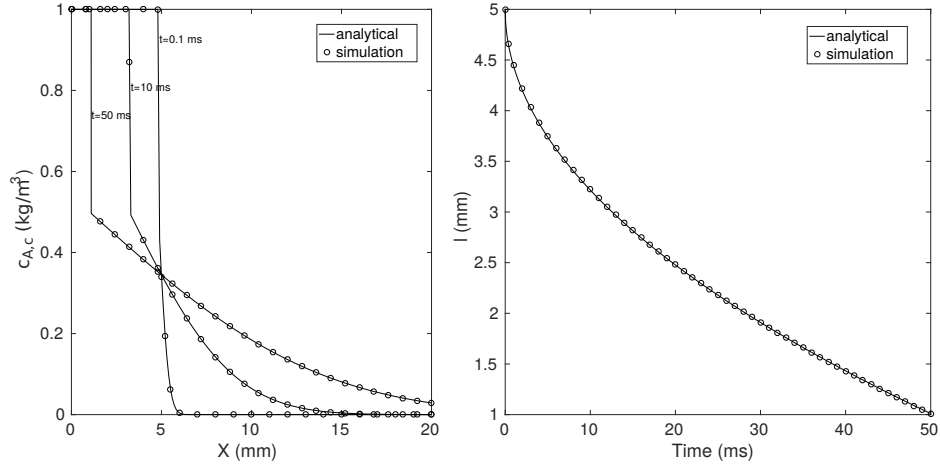


Figure 7: Comparison of analytical and numerical simulation for (a) evolution of species concentration and (b) evolution of interface position during dissolution of a single-component gas phase into an immiscible liquid solvent in a semi-infinite tube. Both concentration and interface position errors are smaller than 0.01.

387 dispersed gas phase is $R_0 = 0.5$ mm, so that the domain is filled with gas for $0 \leq r < R_d$ and with the continuous
 388 liquid phase for $R_d < r < R$ (Fig. 8). The fluid properties are summarised in Table 1.

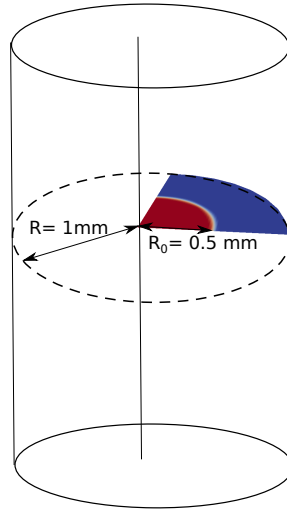


Figure 8: Set-up for growth of binary gas in infinite cylinder.

	Density (kg/m ³)	Dynamic viscosity (Pa.s)	Interfacial tension (mN/m)
Gas	1	1.8×10^{-5}	60
Liquid	1000	1×10^{-3}	

Table 1: Fluid properties for mass transfer during growth of binary gas in infinite cylinder

389 We consider that the gas is a binary mixture (A+B). Initially, the gas phase is composed at 100% of B ($c_{A,d} = 0$,
 390 $c_{B,d} = \rho_d$). We assume that A is only weakly soluble ($H_A = 0.01$) and B is not soluble ($H_B = 0$) in liquid, so that
 391 the liquid phase is a binary mixture of A and a solvent that is not soluble in the gas phase. The diffusion coefficient
 392 are $D_{A,d} = D_{B,d} = 10^{-4}$ m²/s and $D_{A,c} = D_{B,c} = 10^{-6}$ m²/s. At the outside boundary of the system, the pressure

393 remains constant, and the concentration of A is equal to $H_A \rho_d$. Due to the symmetry of the problem, the velocity
 394 and concentration only depends on the radius r , and the motion induced in the liquid phase is also radial,

$$\mathbf{w} = w(t) \vec{e}_r, \quad \mathbf{u}_c = u_c(r, t) \vec{e}_r. \quad (57)$$

Since $\rho_d \ll \rho_c$, mass conservation at the interface (Eq. (2)) gives

$$u_c(R_d, t) = w(t). \quad (58)$$

395 Due to the large diffusion ratio between the gas and liquid phases, the species concentration in the gas phase can
 396 be considered uniform at the time scale of the process. Since the total mass of B is a constant, the concentration
 397 of A in the gas phase satisfies

$$c_{A,d} = \rho_d \left(1 - \left(\frac{R_0}{R_d} \right)^2 \right). \quad (59)$$

398 Mass conservation of the dilute component in the liquid phase writes

$$\begin{aligned} \frac{\partial c_{A,c}}{\partial t} + u_c \frac{\partial c_{A,c}}{\partial r} &= \frac{D_{A,c}}{r} \frac{\partial}{\partial r} \left(r \frac{\partial c_{A,c}}{\partial r} \right) && \text{for } r > R_d, \\ u_c(r, t) &= \frac{R_d}{r} w(t) && \text{for } r > R_d, \\ c_{A,c}(R_d, t) &= H_A \rho_d \left(1 - \left(\frac{R_0}{R_d} \right)^2 \right), \quad c_{A,c}(R, t) = H_A \rho_d && \text{for } t > 0, \\ \frac{dR_d}{dt} = w &= \frac{D_{A,c}}{\rho_d} \frac{\partial c_{A,c}}{\partial r} \Big|_{r=R_d} && \text{for } t > 0. \end{aligned} \quad (60)$$

399 Eq. (60) can be written in its dimensionless form using

$$r^* = \frac{r}{R}, \quad R_d^* = \frac{R_d}{R}, \quad t^* = \frac{t}{\tau}, \quad c^* = \frac{c_{A,c}}{H_A \rho_d}, \quad (61)$$

where asterisks denote dimensionless variables and

$$\tau = \frac{R^2}{H_A D_{A,c}}. \quad (62)$$

400 The time-scale τ corresponds to the time it takes a mass $\pi \rho_d R^2 L$ in a cylinder of radius R and length L to diffuse
 401 out of the system if the mass flux density is $D_{A,c} L \pi H_A \rho_d$. For $D_{A,c} = 10^{-6} \text{ m}^2/\text{s}$, $\tau = 100 \text{ s}$. Substituting into
 402 Eq. (60) yields

$$\begin{aligned} H_A \left(\frac{\partial c^*}{\partial t^*} + w^* \frac{R_d^*}{r^*} \frac{\partial c^*}{\partial r^*} \right) &= \frac{1}{r^*} \frac{\partial}{\partial r^*} \left(r^* \frac{\partial c^*}{\partial r^*} \right) && \text{for } r^* > R_d^*, \\ c^*(R_d^*, t^*) &= 1 - \left(\frac{R_d^*(0)}{R_d^*} \right)^2, \quad c^*(1, t^*) = 1 && \text{for } t^* > 0, \\ \frac{dR_d^*}{dt^*} = w^* &= \frac{\partial c^*}{\partial r^*} \Big|_{r^*=R_d^*} && \text{for } t^* > 0 \end{aligned} \quad (63)$$

403 Since $H_A \ll 1$, the concentration of A in the liquid phase can be assumed at equilibrium at the time-scale of the

404 motion of the interface. Therefore, Eq. (63) becomes

$$\begin{aligned} \frac{1}{r^*} \frac{\partial}{\partial r^*} \left(r^* \frac{\partial c^*}{\partial r^*} \right) &= 0 && \text{for } r^* > R_d^*, \\ c^*(R_d^*, t^*) &= 1 - \left(\frac{R_d^*(0)}{R_d^*} \right)^2, \quad c^*(1, t^*) = 1 && \text{for } t^* > 0, \\ \frac{dR_d^*}{dt^*} &= w^* = \frac{\partial c^*}{\partial r^*} \Big|_{r^*=R_d^*} && \text{for } t^* > 0 \end{aligned} \quad (64)$$

405 An analytical solution for Eq. (64) writes

$$\begin{aligned} c_{A,c}(r, t) &= H_A \rho_d \left(1 - \left(\frac{R_0}{R_d} \right)^2 \frac{\ln(r/R)}{\ln(R_d/R)} \right), \text{ for } r > R_d, \\ \frac{1}{4} \left(R_d^4 \ln \left(\frac{R_d}{R} \right) - R_0^4 \ln \left(\frac{R_0}{R} \right) \right) - \frac{1}{16} (R_d^4 - R_0^4) &= -R_0^2 H_A D_{A,c} t, \text{ for } t > 0. \end{aligned} \quad (65)$$

406 The simulations are performed in 2D on a quarter-circle, using symmetry condition on the left and bottom bound-
407 aries. In order to investigate convergence, we define the dimensionless grid size

$$\Delta x^* = \frac{\Delta x}{R}, \quad (66)$$

408 and the error for concentration and gas radius

$$\begin{aligned} \text{Err}(c(\Delta x^*)) &= \max_t \left(\sqrt{\int \left(\frac{c_{A,c}(\Delta x^*, t) - c_{A,c}(\Delta x^* \rightarrow 0, t)}{H_A \rho_d} \right)^2 dt} \right), \\ \text{Err}(R_d(\Delta x^*)) &= \max_t \left(\frac{|R_d(\Delta x^*, t) - R_d(\Delta x^* \rightarrow 0, t)|}{R_d(0)} \right). \end{aligned} \quad (67)$$

409 The domain is first meshed with a uniform Cartesian grid, then all cells containing solid are removed and re-
410 placed by rectangular and triangular cells that match the solid boundaries, using the OpenFOAM[®] utilities *snap-*
411 *pyHexMesh* (OpenCFD, 2016). Fig. 9 shows the evolution of the convergence errors with grid resolution. All
simulations are performed with a time-step of 0.1 μ s, for which they have all converged in time. Again, we ob-

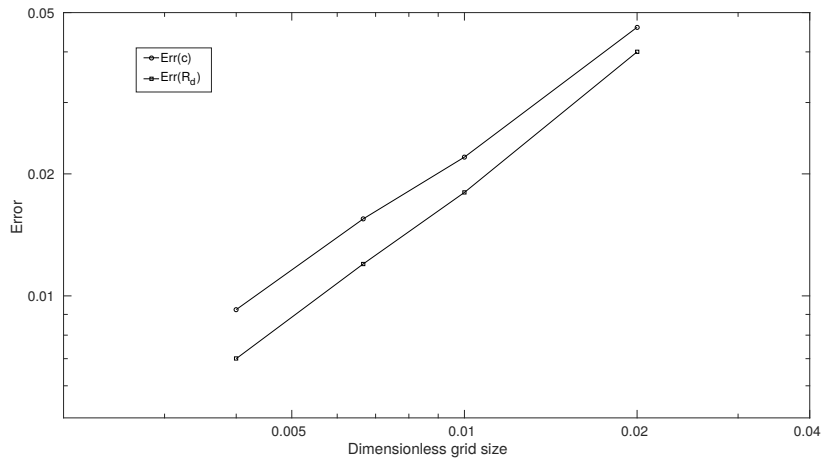


Figure 9: Evolution of convergence of concentration and gas radius during growth of binary gas in infinite cylinder. Both measures show first-order convergence.

413 serve that both measures show first-order convergence, due to the first-order upwinding discretization of the phase
 414 transfer flux (Eq. 46).

415 Fig. 10 shows the evolution of the dimensionless concentration of component A and of the gas-liquid interface,
 416 for a grid resolution of $\Delta x^* = 4 \times 10^{-3}$, obtain using *snappyHexMesh* with an initial Cartesian grid of 250×250 .
 The final grid contains 46801 cells.

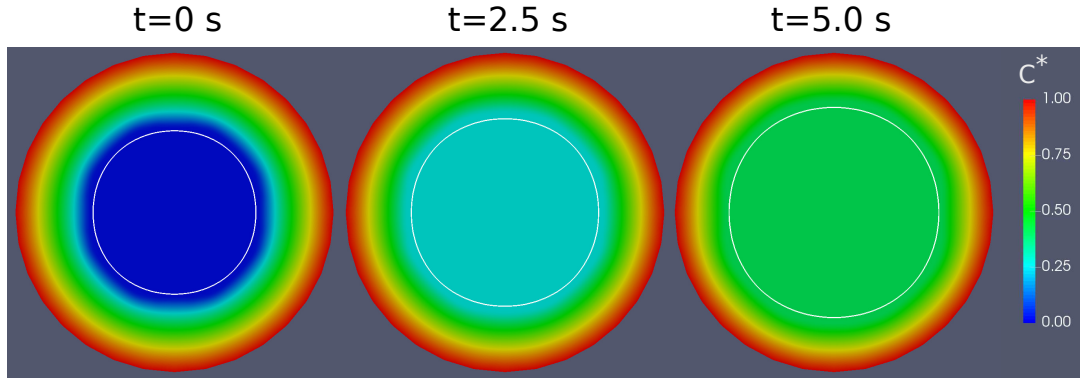


Figure 10: Evolution of dimensionless concentration of component A (colour map) and of gas-liquid interface (white curve) during growth of binary gas in infinite cylinder.

417 We observe that the volume of gas grows as component A diffuses across the interface. Fig. 11 shows
 418 a comparison between numerical and analytical solution for the dimensionless concentration and radius. The
 419 observed errors (9×10^{-3} for concentration, 7×10^{-3} for radius) are due to the difficulty of maintaining a sharp
 420 interface. In addition, we observe that the curvature of the interface is not perfectly circular (Fig. 10). In fact,
 421 it oscillates slightly during the simulation due to parasitic currents. In our work, the impact of these spurious
 422 currents is only limited and smoothing the indicator function prior to the computation of interface curvature is
 423 enough to limit them. To increase robustness and accuracy, various techniques to reduce them further can be
 424 considered, such as sharpening of indicator function prior to surface tension force computation (Francois et al.,
 425 2006), filtering of capillary force (Raeini et al., 2012) or coupled VOF level-set method (Albadawi et al., 2013),
 426 but are outside the scope of this work.

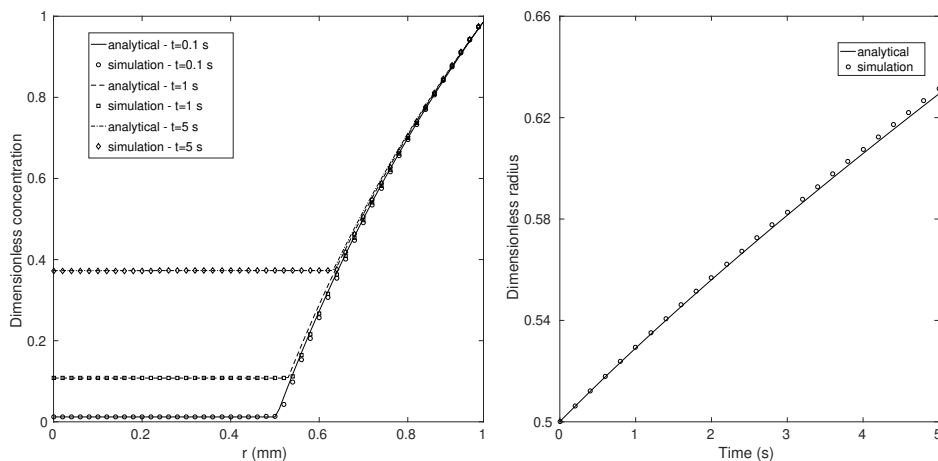


Figure 11: Comparison between numerical and analytical solution for the dimensionless concentration and dimensionless radius during growth of binary gas in infinite cylinder.

3.4. Mass transfer from a single-component rising gas bubble in creeping flow

The objective of this test case is to validate the interface mass transfer in a 3D geometry with dynamic motion of the interface, on both structured and unstructured grids. For this, we consider the rising of a 3D gas bubble in the creeping flow regime ($Re \ll 1$). Although no analytical solution of the full species equation for this problem is available, Fleckenstein and Bothe (2015) proposed a semi-analytical method to solve the mass transfer across the interface. This uses the Hadamard-Rybczynski analytical solution (Hadamard, 1911) of flow around a spherical bubble at low Reynolds number. In spherical coordinate and in a reference frame moving with the barycentre of the bubble, the velocity field is given by

$$\begin{aligned} u_{rad} &= -U_b \left(1 - \frac{1.5\mu_d/\mu_c + 1}{\mu_d/\mu_c + 1} \frac{1}{r/R} + \frac{\mu_d/\mu_c}{\mu_d/\mu_c + 1} \frac{1}{(r/R)^3} \right) \cos \theta, \\ u_\theta &= U_b \left(1 - \frac{1.5\mu_d/\mu_c + 1}{\mu_d/\mu_c + 1} \frac{1}{2r/R} + \frac{\mu_d/\mu_c}{\mu_d/\mu_c + 1} \frac{1}{2(r/R)^3} \right) \sin \theta, \end{aligned} \quad (68)$$

where u_{rad} and u_θ are the radial and tangential components of the velocity, R is the radius of the bubble and U_b is the bubble rising velocity, given by

$$U_b = \frac{2}{3} \frac{\rho_d - \rho_c}{\mu_c} g R^2 \frac{1 + \mu_d/\mu_c}{2 + 3\mu_d/\mu_c}. \quad (69)$$

Then, assuming rotational symmetry, the stationary species equation in the continuous phase is given by

$$u_r \frac{\partial c}{\partial r} + u_\theta \frac{1}{r} \frac{\partial c}{\partial \theta} = D \left(\frac{1}{r^2} \frac{\partial}{\partial r} \left(r^2 \frac{\partial c}{\partial r} \right) + \frac{1}{\sin \theta} \frac{\partial}{\partial \theta} \left(\sin \theta \frac{\partial c}{\partial \theta} \right) \right). \quad (70)$$

Fleckenstein and Bothe (2015) numerically solves a simplified form of Eq. (70) that neglects the last term on the right-hand side by assuming good mixing along the streamline, then computes the interface mass transfer to update the bubble radius R .

Mass transfer from a single-component gas bubble has been simulated and compared to the semi-analytical solution. The fluid properties are summarised in Table 2. A Henry's coefficient of 0.2 is chosen. A bubble with

	Density (kg/m^3)	Dynamic viscosity (Pa.s)	Diffusivity (m^2/s)	Interfacial tension (mN/m)
Gas	1.2	1.8×10^{-5}	0	60
Liquid	1245	0.46	1.48×10^{-6}	

Table 2: Fluid properties for mass transfer from gas bubble in creeping flow

initial radius $R = 2$ mm has been simulated in a computational domain of dimension $1.2 \text{ cm} \times 2.4 \text{ cm} \times 1.2 \text{ cm}$. Symmetry conditions are applied to the plan $x=0$ and $z=0$, so only a quarter of the bubble is simulated. The other boundary conditions are free-flow.

Two different grids are considered here, a structured one and an unstructured one. The structured grid is obtained by meshing the computational domain uniformly with $150 \times 300 \times 150$ cells. For the unstructured grid, a tetrahedral mesh is first obtained using the open source software gmsh (Geuzaine and Remacle, 2009) by extruding a 2D triangular mesh. Then, the OpenFOAM[®] *polyDualMesh* utility (OpenCFD, 2016) is used to convert to a polyhedral mesh. In order to obtain a similar number of cells for both grids, the resolution of the triangular mesh is set to 9.23×10^{-5} m (260 points per direction). The final grids contain 6.75 million cells for the structured mesh and 6.81 million cells for the unstructured mesh.

The simulations were run with a constant time-step of $20 \mu\text{s}$. Initially, the centre of the bubble is placed at (0 mm, 3 mm, 0 mm). In order to compare with the semi-analytical, mass transfer from a rising bubble with no volume change and while forcing the species concentration in the bubble, and therefore the density, to remain constant is simulated until the barycentre of the bubble reaches (0 cm, 1.2 cm, 0 cm). The simulations are then

458 restarted with local volume change taken into account. Fig. 12 shows the interface position and the dimensionless
 459 concentration $c^* = c / (\alpha + H(1 - \alpha))$ profile at $t=0.2$ s, for both structured and unstructured grids. The profile are

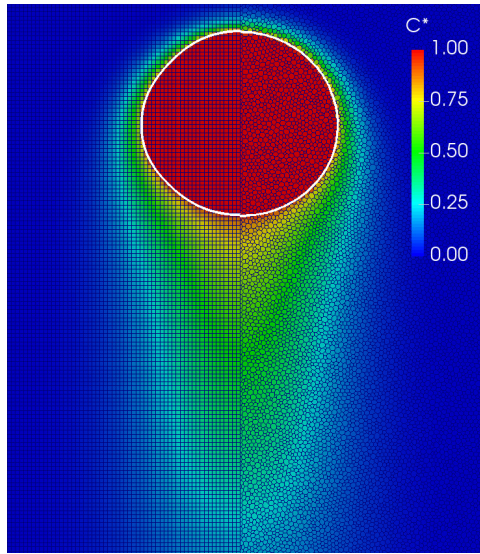


Figure 12: Interface position (white line) and dimensionless concentration profile at $t=0.2$ s for both structured and unstructured grids during rising of a gas bubble in creeping flow.

459
 460 very similar. The unstructured solution is slightly more diffuse, and the bubble velocity slightly reduced, but the
 461 difference is not significant.

462 At $t=0$, the rising velocity obtained in the simulation is equal to 3.0 cm/s, while the exact velocity obtained
 463 with the Hadamard-Rybczynski solution is approximately 3.5 cm/s. Similarly to Fleckenstein and Bothe (2015),
 464 Eq. (70) is adjusted for the semi-analytical computation to account for this discrepancy. Fig. 13 shows the
 465 evolution of the normalised mass of gas obtained with the numerical model and compared to the semi-analytical
 466 solution. After a total simulated time of 0.25 s, the mass has decreased to 81% of its initial value in the structured
 467 grid simulation, 81.4% in the unstructured grid simulation, and to 80.6% of its initial value in the semi-analytical
 468 solution. This corresponds to a relative deviation of 0.5% for the structured grid and 1% for the unstructured grid
 469 at the end of the simulation.

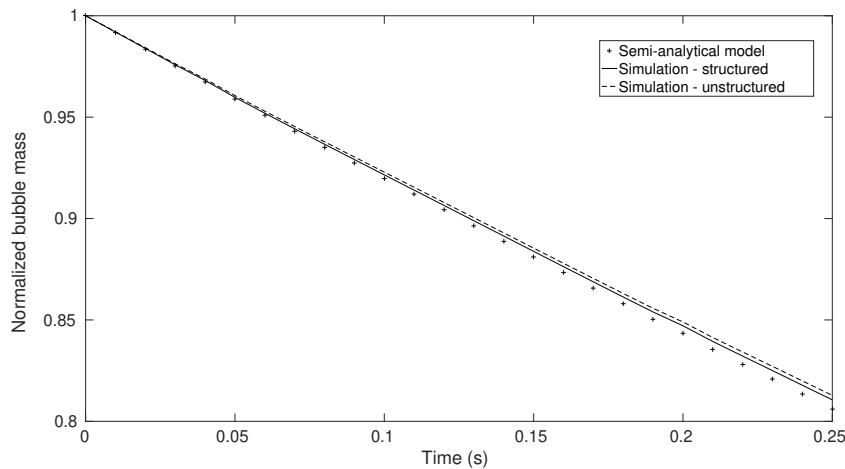


Figure 13: Comparison of semi-analytical model and numerical simulation for normalised total mass of gas during rising of a gas bubble in creeping flow.

470 4. Application

471 4.1. Competing mass transfer in infinite cylinder

472 In industrial applications involving mass transfer at fluid interfaces, species being transferred from the gas
 473 phase to the liquid phase and species being transferred in the opposite direction can both happen simultaneously.
 474 This competing mass transfer directly affect the volume of each phase and must be taken into account in any
 475 numerical modelling.

476 Here, we consider competing mass transfer with two species A and B in an infinite cylinder of radius $R=1$ mm.
 477 The solvent of the continuous phase is not soluble in the disperse phase. The fluid properties (Table 1) and the
 478 geometry (Fig. 8) are the same as in section 3.3, with the initial radius of the dispersed gas phase $R_0 = 0.5$ mm,
 479 so that the domain is filled with gas for $0 \leq r < R_0$ and with liquid for $R_0 < r < R$.

480 Initially, the gas phase is composed at 100% of B ($c_{A,d} = 0$, $c_{B,d} = \rho_d = 1$ kg/m³), and the liquid phase is
 481 at chemical equilibrium with the gas phase ($c_{A,c} = 0$, $c_{B,c} = H_B \rho_d$). The diffusion coefficient are $D_{A,d} = D_{B,d} =$
 482 10^{-4} m²/s and $D_{A,c} = D_{B,c} = 10^{-6}$ m²/s. At the outside boundary of the system, the pressure remains constant, the
 483 concentration of B is equal to 0 and the concentration of A is equal to $H_A \rho_d$.

484 Like in section 3.3, the simulations are performed on a quarter-circle. The domain is represented by a 50×50
 485 uniform Cartesian mesh. All cells containing solid are removed and replaced by rectangular and triangular cells
 486 that match the solid boundaries. The final grid contains 1875 cells. The simulation is run with a constant time-step
 487 of 1μ s. We consider four cases, with $H_A = 1.0, 0.5$ and $H_B = 1.0, 0.5$. The evolution of the mass fraction of A and
 488 B in the gas phase as well as the evolution of the gas phase radius R_d in each case are plotted in Fig. 14.

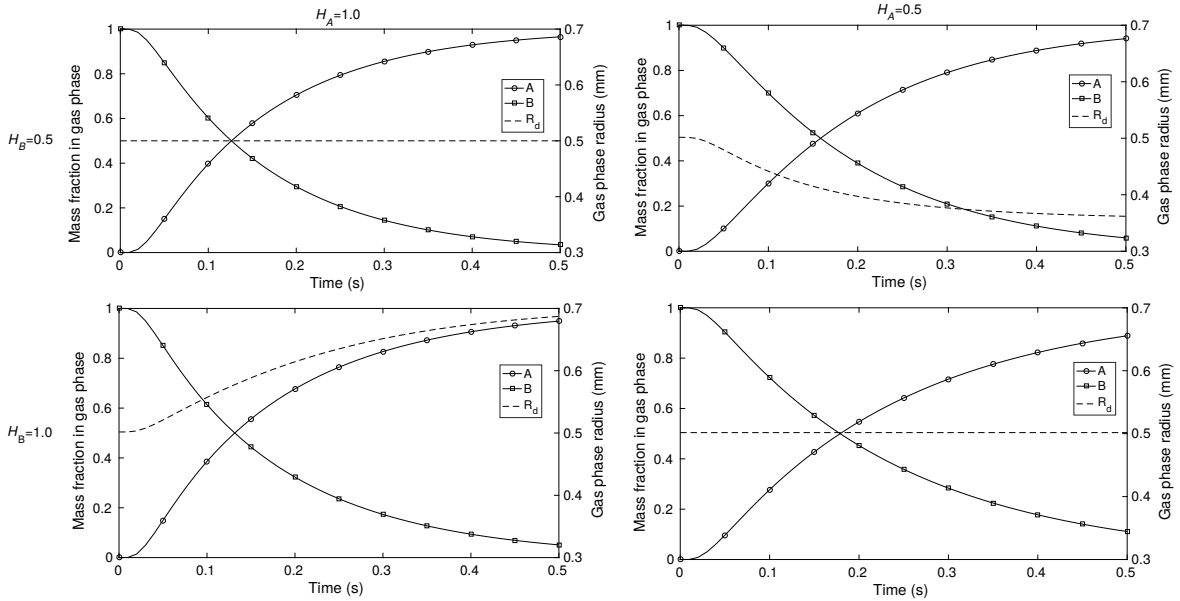


Figure 14: Evolution of mass fraction in gas phase and of gas phase radius during competing mass transfer in infinite cylinder of two component A and B with $H_A = 1, 0.5$ and $H_B = 1, 0.5$.

489 We observe that when $H_A = H_B = 1.0$ and $H_A = H_B = 0.5$, the radius of the gas phase remains constant. That
 490 is because when $H_A = H_B = H$, the sum of the concentration of A and B in the liquid phase is a constant equal
 491 to $H\rho_d$. In this case, the mass transfer fluxes at the interface are exactly opposite, and the volume of gas remains
 492 unchanged.

493 For the two cases when $H_A \neq H_B$, the total mass transfer is equal to zero at $t=0$, since the system is initially
 494 at chemical equilibrium, but as component A diffuses toward the centre of the cylinder and component B diffuses

away from the centre of the cylinder, the chemical balance is modified and the volume of gas change. When $H_A < H_B$, the gas phase recedes and when $H_A > H_B$, the gas phase grows. In both case, we observe that from $t=0.02$ s to $t=0.1$ s, the slope is maximum and the radius changes almost linearly with time. This is because the fraction of A in the gas phase is still marginal. With increasing time, the composition of the gas phase changes significantly. As the system evolves toward chemical equilibrium for component A , the rate of volume change decreases.

Additional multi-physics need to be included in order to model the full behaviour of the system, such as gas compressibility and pressure/temperature dependent equilibrium constant. This shall be investigated in future work.

4.2. Mass transfer during rising of a single-component gas bubble at low Schmidt number

In this section, the impact of the local volume change on the Sherwood number during the rising of a single-component gas bubble at low Schmidt number is investigated. Two cases are considered and the fluid properties are summarised in Table 3. For test case 1, we consider a domain of size $1.2 \text{ cm} \times 2.4 \text{ cm} \times 1.2 \text{ cm}$. A gas bubble

	Density (kg/m^3)	Dynamic viscosity (Pa.s)	Diffusivity (m^2/s)	Interfacial tension (mN/m)
Gas	1.2	1.8×10^{-5}	0	65
Liquid 1	1200	0.024	2×10^{-5}	
Liquid 2	1200	0.46	3.83×10^{-4}	

Table 3: Fluid properties for mass transfer for rising of single-component gas bubble at low Schmidt number

of radius $R = 2 \text{ mm}$ is immersed in liquid 1 (Table 3). The Eötvös number can be calculated using the diameter of the bubble as a reference length and we find $Eo=3$. The Morton number is independent of the bubble size and $Mo=10^{-5}$. For these values, Clift’s diagram describing the shape regime (Clift et al., 1978) predicts an ellipsoidal shape and a Reynolds number around 30. The bubble is initially at capillary equilibrium in the absence of gravity and interface mass transfer, with centre placed at $(0 \text{ cm}, 0.3 \text{ cm}, 0 \text{ cm})$.

For test case 2, the domain considered and the gas bubble are five time larger ($R=10 \text{ mm}$), and the bubble is immersed in liquid 2 (Table 3). The Eötvös and Morton numbers are 70 and 1.3, respectively. For these values, Clift’s diagram (Clift et al., 1978) predicts a dimpled ellipsoidal-cap shape and a Reynolds number around 10. Again, the bubble is initially at capillary equilibrium in the absence of gravity and interface mass transfer, with centre placed at $(0 \text{ cm}, 1.5 \text{ cm}, 0 \text{ cm})$.

At $t=0$, gravity and interface transfer are “turned on”. The bubble starts rising and shrinking. Note that in both case, the diffusivity coefficient in the liquid phase corresponds to a Schmidt number $Sc=1.0$.

Like in section 3.4, symmetry conditions are applied to the plan $x=0$ and $z=0$, so only a quarter of the bubble is simulated. The other boundary conditions are free-flow. The computational domain is resolved uniformly with $150 \times 300 \times 150$ cells. The simulation is run with a constant time-step of $20 \mu\text{s}$ for case 1 and $100 \mu\text{s}$ for case 2. For each case, we consider two possible values of H : one with $H = 0.01$, so the species is only weakly dilute in the liquid phase, and one with a larger Henry’s coefficient $H = 0.2$. Fig. 15 show the evolution of the phase fraction during the simulations and Fig. 16 shows the species dimensionless concentration $c^* = c / (\alpha + H(1 - \alpha))$ at the end of the simulation ($t=0.12 \text{ s}$ for case 1, $t=0.4 \text{ s}$ for case 2). For $H = 0.01$, the bubble deforms as it rises. For case 1, it reaches an ellipsoidal shape at $t=0.05 \text{ s}$, and for case 2, it reaches a dimpled ellipsoidal-cap shape at $t=0.1 \text{ s}$. The impact of the bubble shape on its total surface is quantified using the shape factor Sr , defined as

$$Sr = \frac{A_{\Sigma}}{A_{\text{sphere}}}. \quad (71)$$

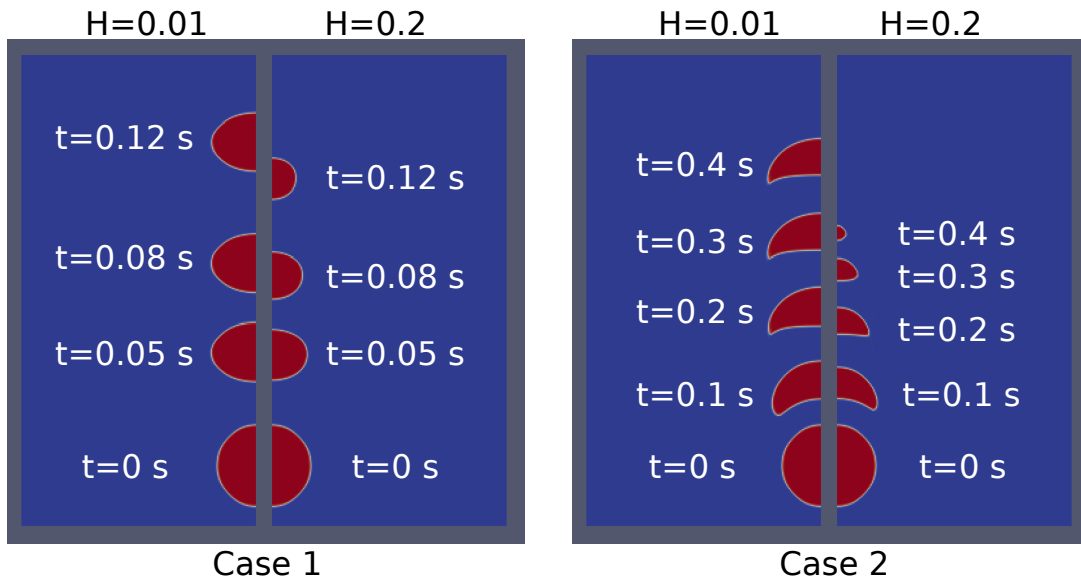


Figure 15: Evolution of phase distribution during rising of a gas bubble for case 1 and 2, $H=0.01$ and $H=0.2$.

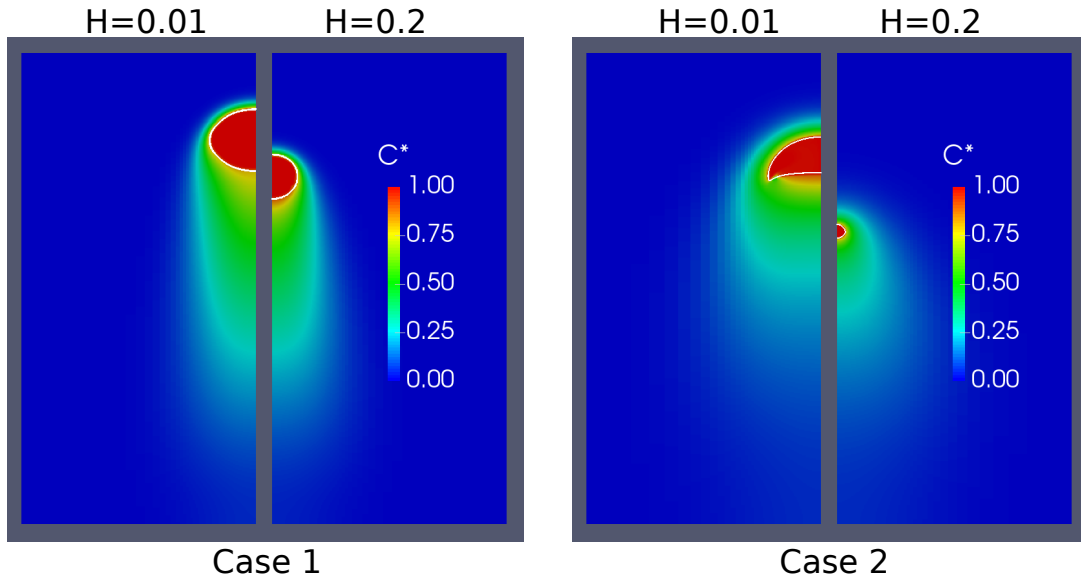


Figure 16: Species dimensionless concentration during rising of a gas bubble for case 1 ($t=0.12$ s) and case 2 ($t=0.4$ s), $H=0.01$ and $H=0.2$.

The shape factor reaches a value of 1.04 for case 1 and 1.38 for case 2. Fig. 17 shows the evolution of the Reynolds number during the simulations. The velocity of the bubble reaches a maximum of 0.155 m/s for case 1 and 0.19 m/s for case 2, which corresponds to Reynolds number $Re=31$ and $Re=9.9$. For $H = 0.01$, the total loss of bubble volume at the end of the simulation is only 6% for case 1 and 8% for case 2, so the local volume change has a limited impact on the Reynolds number. The Sherwood number is obtained by computing the mass exchange coefficient k using Eq. (50). The numerical results are plotted in Fig. 18 and compared to the correlations proposed

by Oellrich et al. (1973), with a shape factor correction (Deising et al., 2018)

$$\text{Sh.Sr} = 2 + 0.651 \frac{\text{Pe}^{1.72}}{1 + \text{Pe}^{1.22}} \quad \text{if } Re \rightarrow 0 \text{ and } Sc \rightarrow \infty \quad (72)$$

$$\text{Sh.Sr} = 2 + 0.232 \frac{\text{Pe}^{1.72}}{1 + 0.205\text{Pe}^{1.22}} \quad \text{if } Re \rightarrow \infty \text{ and } Sc \rightarrow 0 \quad (73)$$

529 We observe that the numerical results are closer to the case $Re \rightarrow 0$, $Sc \rightarrow \infty$, which suggests that Eq. (72) is valid
 530 for a larger parameter range. This was previously observed for mass transfer with no local volume change (Bothe
 531 and Fleckenstein, 2013; Deising et al., 2018).

532 For $H = 0.2$, the bubble also deforms as it rises but, as gas dissolves in the liquid phase, the volume of the
 533 bubble decreases and so the Eötvös number decreases as well. For case 1, Eo is equal to 1.98 at $t=0.05$ s, 1.55
 534 at $t=0.08$ s and 1.0 at $t=0.12$ s. For these values, Clift's diagram (Clift et al., 1978) predicts a transition from
 535 ellipsoidal to spherical shape, which is observed in Fig. 15. The shape factor Sr is equal to 1.03 at $t= 0.05$ s, 1.02
 536 at $t=0.08$ s and 1.01 at $t=0.12$ s. The total loss of bubble volume at the end of the simulation is 79%. For case
 537 2, Eo is equal to 45 at $t=0.1$ s, 27 at $t=0.2$ s, 13 at $t=0.3$ s and 3.3 at $t=0.4$ s. For these values, Clift's diagram
 538 (Clift et al., 1978) predicts a transition from dimpled ellipsoidal-cap to ellipsoidal shape and then from ellipsoidal
 539 to spherical shape, which is observed in Fig. 15. The shape factor Sr is equal 1.30 at $t=0.1$ s, 1.22 at $t=0.2$ s, 1.10
 540 at $t=0.3$ s and 1.08 at $t=0.4$ s. The total loss of bubble volume at the end of the simulation is 99%.

541 Moreover, the bubble velocity decreases as it dissolves. Fig. 17 shows the evolution of the Reynolds number
 542 during the simulations. We observe that the bubble does not reach the same maximum Reynolds ($Re=31$ for case
 543 1 and $Re=10$ for case 2) as for $H = 0.01$. Instead, the Reynolds reaches a maximum $Re=24$ at $t=0.04$ s for case
 544 1 and $Re=8.9$ at $t=0.08$ s for case 2, and then decreases almost linearly. Fig. 18 shows a comparison between the
 Sherwood number numerically obtained and the ones obtained from Oellrich correlations (Eqs. (72) and (73)).

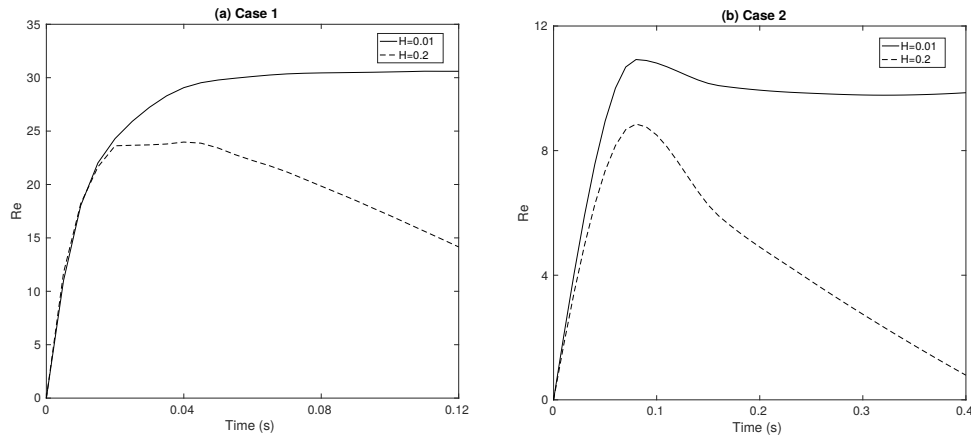


Figure 17: Evolution of Reynolds number during rising of a gas bubble for case 1 and 2, $H=0.01$ and $H=0.2$.

545 Again, we observe that the numerical results are closer to the case $Re \rightarrow 0$, $Sc \rightarrow \infty$. Moreover, the trend of
 546 the Sherwood number which decreases as the bubble volume decreases is accurately represented. This suggests
 547 that the impact of local volume change on Sherwood number might be accurately described by using the time-
 548 dependent Reynolds number in the same integral correlations.
 549

550 5. Conclusion

551 In this paper, a novel unified single-field formulation for Volume-Of-Fluid simulation of interfacial mass trans-
 552 fer with local volume changes has been presented. The main focus of this work is a rigorous derivation of the

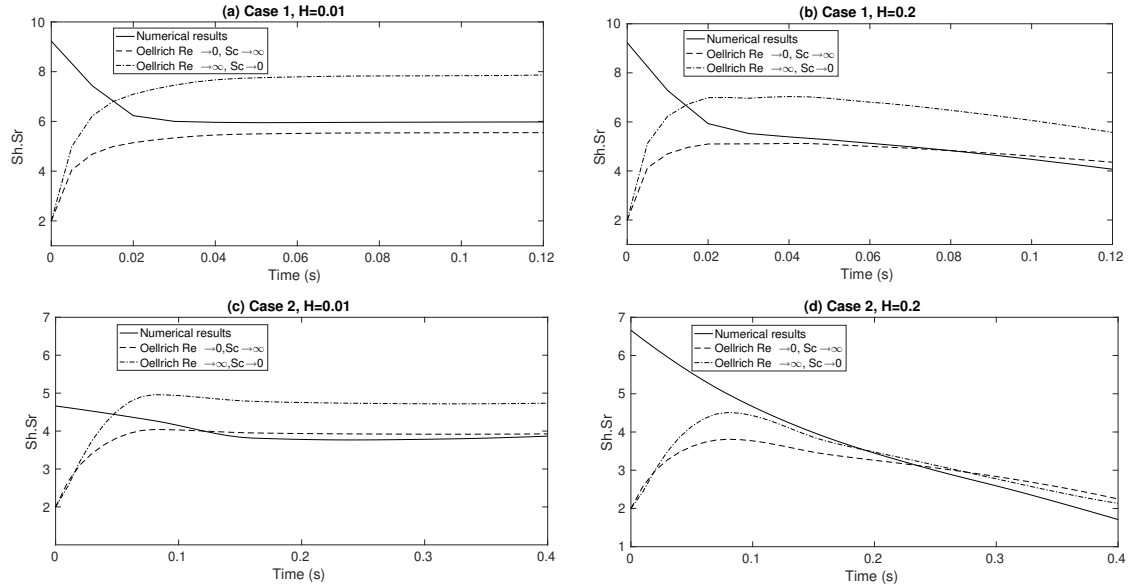


Figure 18: Evolution of Sherwood number and comparison with Oellrich correlation during rising of a gas bubble for case 1 and 2, $H=0.01$ and $H=0.2$.

single-field local mass transfer between phases at the interface, which is re-injected in the phase conservation equation. To compute this mass transfer and the local volume change, both convective and diffusive contribution are considered. The single-field formulation couples the mass and momentum transfer via a source term in the pressure equation.

The numerical method is validated by comparison with four test cases. For the first test case, artificial mass transfer is evaluated for a case with infinite Péclet number, and we observed consistency between advection of phase fraction and advection of species concentration in the case of an algebraic VOF method with compression of the interface using the normal C-CST method. For the second and third test cases, analytical solutions of the dissolution of a single-component gas phase into an immiscible liquid solvent in a semi-infinite tube and of the growth of a binary gas phase in an infinite cylinder are considered. For the last test case, we use the semi-analytical solution described by Fleckenstein and Bothe (2015) for the mass transfer across the interface of a rising gas bubble in the creeping flow regime. A very good agreement of the numerical results with the reference solution is obtained in each case. The main weakness of the approach is the first-order accurate discretization of the interface transfer \dot{m} . Additional research is needed to develop a bounded second-order discretization.

The validated approach is first applied to investigate competing mass transfer between two species A and B in an infinite cylinder. The simulation was able to reproduce the direction of the gas/liquid interface motion for various cases where $H_A = H_B$, $H_A < H_B$ and $H_B < H_A$, as well as the impact of total mass fraction in the bubble. In future work, additional multi-physics such as gas compressibility and pressure/temperature dependent equilibrium constant will be included.

Finally, the method is applied to investigate mass transfer during the rising of a single-component gas bubble at low Schmidt number. Our results suggests that the impact of local volume change on the Sherwood number might be accurately described by using the time-dependent Reynolds number in the same integral correlations.

By comparison with the two-field method presented by Fleckenstein and Bothe (2015), the advantage of the single-field formulation is that it is fully consistent in principles with any algebraic VOF method, as long as the same discretization schemes are applied for all advected quantities. We showed that within a VOF method with compression of the interface, it can be applied on structured and unstructured grids, with comparable results. In future work, our numerical model will be used to investigate dissolution during geological trapping of CO_2 in

580 aquifers, for which unstructured grids are essential to capture the complex geometry of the porous media and
581 accurately estimate key parameters such as pore surface area (Graveleau et al., 2017; Soulaire et al., 2017).

582 **Acknowledgements**

583 The first author was supported by the UK EPSRC funded project on Direct Numerical Simulation for Additive
584 Manufacturing in Porous Media. The second author was sponsored by the BRGM TRIPHASIQUE project.

585 **Nomenclature**

586 **Variables**

587	A	Area (m^2)
588	c	concentration (kg/m^3)
589	D	molecular diffusivity (m^2/s)
590	F	advective flux ($kg/m^2/s$)
591	f	interior force (N/m^3)
592	g	gravity acceleration (m^2/s)
593	H	Henry constant
594	J	molecular diffusion flux ($kg/m^2/s$)
595	k	mass exchange coefficient (m/s)
596	l	length (m)
597	n	normal vector
598	p	pressure (Pa)
599	r	radius (m)
600	S	Stress tensor ($kg/m/s^2$)
601	t	time (s)
602	u	velocity (m/s)
603	V	Volume (m^3)
604	w	interface velocity (m/s)
605	α	phase volume fraction
606	κ	interface curvature (m^{-1})
607	μ	viscosity ($Pa.s$)
608	Φ	flux ($kg/m^2/s$)
609	ρ	mass density (kg/m^3)

610 σ interfacial tension (N/m)

611 \dot{m} mass transfer (kg/m³/s)

612 **Subscripts**

613 Σ fluid/fluid interface

614 c continuous phase

615 $comp$ compressive

616 d disperse phase

617 f cell phase

618 i phase index

619 j component index

620 n component n, solvent of continuous phase

621 r relative

622 **Abbreviations**

623 C-CST Compressive Continuous Species Transfer

624 CICSAM Compressive Interface Capturing Scheme for Arbitrary Meshes

625 CSF Continuous Surface Force

626 CST Continuous Species Transfer

627 DNS Direct Numerical Simulation

628 FCT Flux Corrected Transfer

629 FVM Finite Volume Method

630 HRIC High Resolution Interface Capturing

631 MULES Multidimensional Universal Limiter with Explicit Solution

632 NSE Navier-Stokes Equations

633 NVF Normalised Variable Formulation

634 PISO Pressure Implicit Sequential Operator

635 VOF Volume-Of-Fluid

636 **References**

- 637 Albadawi, A., Donoghue, D. B., Robinson, A. J., Murray, D. B., Delaure, Y. M. C., 2013. Influence of surface tension implementation in
638 Volume Of Fluid and coupled Volume Of Fluid with Level Set method for bubble growth and detachment. *Int. J. Multiphase Flow* 53,
639 11–28.
- 640 Bothe, D., Fleckenstein, S., 2013. A volume-of-fluid-based method for mass transfer processes at fluid particles. *Chem. Eng. Sci.* 101, 283–
641 302.
- 642 Brackbill, J. U., Kothe, D. B., Zemach, C., 1992. A continuum method for modeling surface tension. *J. Comput. Phys.* 100 (2), 335–354.
- 643 Chai, M., Luo, K., Shao, C., Fan, J., 2017. An efficient level set remedy approach for simulaion of two-phase flow based on sigmoid function.
644 *Chem. Eng. Sci.* 172, 335–352.
- 645 Clift, R., Grace, J. R., Weber, M. E., 1978. Bubbles, drops, and particles. New York; London: Academic Press.
- 646 Coutelieres, F., Kainourgiakis, M., Stubos, A., Kikkinides, E., Yortsos, Y., 2006. Multiphase mass transport with partitioning and inter-phase
647 transport in porous media. *Chem. Eng. Sci.* 61 (14), 4650–4661.
- 648 Danckwerts, P. V., 1970. Gas-liquid reaction. McGraw-Hill, New-York, New-York.
- 649 Deising, D., Bothe, D., Marschall, H., 2018. Direct numerical simulation of mass transfer in bubbly flows. *Computer and Fluids* 172, 524–537.
- 650 Deising, D., Marschall, H., Bothe, D., 2016. A unified single-field model framework for Volume-Of-Fluid simulations of interfacial species
651 transfer applied to bubbly flow. *Chem. Eng. Sci.* 139, 173–195.
- 652 Fleckenstein, S., Bothe, D., 2015. A volume-of-fluid-based numerical method for multi-component mass transfer with local volume changes.
653 *J. Comput. Phys.* 301, 35–58.
- 654 Francois, M. M., Cummins, S. J., Dendy, E. D., Kothe, D. B., Sicilan, J. M., Williams, M. W., 2006. A balanced-force algorithm for continuous
655 and sharp interfacial surface tension models within a volume tracking framework. *J. Comput. Phys.* 213 (1), 141–173.
- 656 Gerlach, D., Tomar, G., Biswas, G., Durst, F., 2006. Comparison of volume-of-fluid method for surface tension-dominant two-phase flows.
657 *Int. J. Heat Mass Transfer* 49, 740–754.
- 658 Geuzaine, C., Remacle, J.-F., 2009. Gmsh: A 3-d finite element mesh generator with built-in pre-and post-processing facilities. *International*
659 *Journal for Numerical Methods in Engineering* 79 (11), 1309–1331.
- 660 Gibou, F., Fedkiw, R., Osher, S., 2018. A review of level-set method and some recent applications. *J. Comput. Phys.* 353, 82–109.
- 661 Graveleau, M., Soulaire, C., Tchepeli, H., 2017. Pore scale simulation of interface multicomponent mass transfer for subsurface flow. *Transport*
662 *in porous media* 120 (2), 287–308.
- 663 Hadamard, J., 1911. Mouvement permanent lent d’une sphère liquide et visqueuse dans un liquide visqueux. *C.R. Acad. Sci. Paris* 152,
664 1735–1738.
- 665 Haroun, Y., Legendre, D., Raynal, L., 2010. Volume of fluid method for interfacial reactive mass transfer: Application to stable liquid film.
666 *Chem. Eng. Sci.* 65 (10), 2896–2909.
- 667 Hirt, C. W., Nichols, B. D., 1981. Volume-Of-Fluid (VOF) method for the dynamic of free boundaries. *J. Comput. Phys.* 39 (1), 201–225.
- 668 Issa, R., Ahmadi-Befru, B., Beshay, K., Gosman, A., 1985. Solution of the implicitly discretised reacting flow equations by operator-splitting.
669 *J. Comput. Phys.* 93 (2), 388–410.
- 670 Leonard, B. P., 1988. Universal limiter for transient interpolation modeling of the advective transport equations: the ultimate conservative
671 differencing scheme. NASA Technical Memorandum 100916.
- 672 Luo, K., Shao, C., Chai, M., Fan, J., 2019. Level set method for atomization and evaporation simulations. *Progress in Energy and Combustion*
673 *Science* 50, 49–75.
- 674 Maes, J., Geiger, S., 2018. Direct pore scale reactive transport modelling of dynamic wettability changes induced by surface complexation in
675 carbonate rocks. *Adv. iWater Resour.* 111, 6–19.
- 676 Maes, J., Soulaire, C., 2018. A new compressive scheme to simulate species transfer across fluid interfaces using the volume-of-fluid method.
677 *Chem. Eng. Sci.* 190 (23), 405–418.
- 678 Maric, T., Marschall, H., Bothe, D., 2013. voFoam - A geometrical Volume-Of-Fluid Algorithm on Arbitrary Unstructured Meshes with Local
679 Dynamic Adaptive Mesh Refinement Using OpenFOAM. ArXiv e-prints.
- 680 Marschall, H., Hinterberger, K., Schüler, C., Habla, F., Hinrichsen, O., 2012. Numerical simulation of species transfer across fluid interfaces
681 in free-surface flows using OpenFOAM. *Chemical Engineering Science* 78, 111–127.
- 682 Muzaferija, S., Peric, M., Sames, P., Schellin, T., 1999. A two-fluid navier–stokes solver to simulate water entry. *Twenty-Second Symposium*
683 *on Naval Hydrodynamics*, 638–664.
- 684 Oellrich, H., Schmidt-Traub, H., Brauer, H., 1973. Theoretische berechnung des stofftransports in der umgebung einer einzelblase. *Chem.*
685 *Eng. Sci.* 28, 711–721.
- 686 OpenCFD, 2016. OpenFOAM, the open source cfd toolbox, User Guide. OpenCFD Ltd.
- 687 Owkes, M., Desjardins, O., 2014. A computational framework for conservative, three-dimensional, unsplit, geometric transport with applica-
688 tion to the volume-of-fluid (vof) method. *J. Comput. Phys.* 270, 587–612.
- 689 Patankar, S. V., 1980. *Numerical Heat and Mass Transfer*. Hemisphere Publ. Corp., Washington.
- 690 Popinet, S., 2009. An accurate adaptive solver for surface-tension-driven interfacial flows. *J. Comput. Phys.* 228, 5838–5866.
- 691 Popinet, S., 2018. Numerical models of surface tension. *Annual review of fluid mechanics* 50, 49–76.

692 Quintard, M., Whitaker, S., 1994. Convection, dispersion, and interfacial transport of contaminants: Homogeneous porous media. *Adv. Water*
693 *Resour.* 17 (4), 116–126.

694 Raeini, A., Blunt, M. J., Bijeljic, B., 2012. Modelling two-phase flow in porous media at the pore-scale using the volume-of-fluid method. *J.*
695 *Comput. Phys.* 231 (17), 5653–5668.

696 Rusche, H., 2002. Computational fluid dynamics of dispersed two-phase flows at high phase fraction. Ph.D. thesis, Imperial College London.

697 Scardovelli, R., Zaleski, S., 1999. Direct numerical simulation of free-surface and interfacial flow. *Annu. Rev. Fluid Mech.* 31, 567–603.

698 Soh, G. Y., Yeoh, G. H., Timchenko, V., 2017a. A cfd model for the coupling of multiphase, multicomponent and mass transfer physics for
699 micro-scale simulation. *International Journal of Heat and Mass Transfer* 113, 922–934.

700 Soh, G. Y., Yeoh, G. H., Timchenko, V., 2017b. Numerical investigation of formation and dissolution of co₂ bubbles within silicone oil in
701 cross-junction microchannel. *Microfluid Nanofluid* 21 (175).

702 Soulaine, C., Creux, P., Tchelepi, H. A., 2019. Micro-continuum framework for pore-scale multiphase fluid transport in shale formations.
703 *Transp. Porous Med.* 127 (1), 85–112.

704 Soulaine, C., Debenest, G., Quintard, M., 2011. Upscaling multi-component two-phase flow in porous media with partitioning coefficient.
705 *Chem. Eng. Sci.* 66 (23), 6180–6192.

706 Soulaine, C., Roman, S., Kovscek, A., Tchelepi, H. A., 2017. Mineral dissolution and wormholing from a pore scale perspective. *J. Fluid*
707 *Mech.* 827, 457–483.

708 Soulaine, C., Roman, S., Kovscek, A., Tchelepi, H. A., 2018. Pore-scale modelling of multiphase reactive flow. application to mineral disso-
709 lution with production of co₂. *J. Fluid Mech.* 855, 616–645.

710 Sussman, M., Smereka, P., Osher, S., 1994. A level-set approach for computing solutions to incompressible tow-phase flow. *J. Comput. Phys.*
711 114, 146–159.

712 Takemura, F., Yabe, A., 1998. Gas dissolution process of spherical rising gas bubbles. *Chem. Eng. Sci.* 53 (15), 2691–2699.

713 Taylor, R., Krishna, R., 1993. Multicomponent mass transfer. Vol. 2. John Wiley & Sons.

714 Ubbink, O., Issa, R. I., 1999. A method for capturing sharp fluid interfaces on arbitrary meshes. *J. Comput. Phys.* 153, 26–50.

715 van Leer, B., 1974. Towards the ultimate conservative difference scheme. II. Monotonicity and conservation combined in a second-order
716 scheme. *J. Comput. Phys.* 14 (4), 361–370.

717 Weller, H. G., 2006. A new approach to vof-based interface capturing method for incompressible and compressible flow. Technical Report
718 tOpenCFD Limited.

719 Weymouth, G. D., Yue, D. K. P., 2010. Conservative volume-of-fluid method for free-surface simulations on cartesian grids. *J. Comput. Phys.*
720 229 (8), 2853–2865.

721 Whitaker, S., 1999. The method of volume averaging, theory and applications of transport in porous media. Dordrecht: Kluwer Academic.

722 Yang, L., Nieves-Remacha, M. J., Jensen, K. F., 2017. Simulations and analysis of multiphase transport and reaction in segmented flow
723 microreactors. *Chem. Eng. Sci.* 169, 106–116.

724 Zalesak, S. T., 1979. Fully multidimensional flux-corrected transport algorithm for fluids. *J. Comput. Phys.* 31, 335–362.